MASARYKOVA UNIVERZITA
Přírodovědecká fakulta
Ústav teoretické fyziky a astrofyziky

# Bakalářská práce

Brno 2025 Petra Tereza Bukovinská

MASARYKOVA
UNIVERZITA
PŘÍRODOVĚDECKÁ FAKULTA
ÚSTAV TEORETICKÉ FYZIKY A ASTROFYZIKY

# Proměnnost ultrafialového spektra rentgenové dvojhvězdy HD 49798

Bakalářská práce

**Petra Tereza Bukovinská**

**Vedoucí práce: prof. Mgr. Jiří Krtička, Ph.D** **Brno 2025**

# Bibliografický záznam

| | |
|---|---|
| **Autor:** | Petra Tereza Bukovinská<br>Přírodovědecká fakulta, Masarykova univerzita<br>Ústav teoretické fyziky a astrofyziky |
| **Název práce:** | Proměnnost ultrafialového spektra rentgenové dvojhvězdy HD 49798 |
| **Studijní program:** | Fyzika |
| **Studijní obor:** | Astrofyzika |
| **Vedoucí práce:** | prof. Mgr. Jiří Krtička, Ph.D |
| **Akademický rok:** | 2024/2025 |
| **Počet stran:** | xiii + 51 |
| **Klíčová slova:** | podtrpaslíci; hvězdný vítr; profil P Cygni; HD 49798 |

# Bibliographic Entry

| | |
|---|---|
| **Author:** | Petra Tereza Bukovinská<br>Faculty of Science, Masaryk University<br>Department of Theoretical Physics and Astrophysics |
| **Title of Thesis:** | Ultraviolet spectral variability of X-ray binary HD 49798 |
| **Degree Programme:** | Physics |
| **Field of Study:** | Astrophysics |
| **Supervisor:** | prof. Mgr. Jiří Krtička, Ph.D |
| **Academic Year:** | 2024/2025 |
| **Number of Pages:** | xiii + 51 |
| **Keywords:** | subdwarfs; stellar wind; P Cygni profile; HD 49798 |

# Abstrakt

HD 49798 je jediná známá rentgenová dvojhvězda, kde donorem hmoty je horký podtrpaslík typu O. Jeho společníkem je kompaktní objekt dosud neznámého typu, buďto bílý trpaslík nebo neutronová hvězda, s rychlou rotací $P = 13,2\,\mathrm{s}$ a stálým zrychlením rotace $\dot{P} = -2.28 \times 10^{-15}\,\mathrm{s\,s^{-1}}$. Díky aktivitě hvězdného větru a akreci dvojhvězda vykazuje významný rentgenový zářivý výkon $L_X \approx 10^{32}\,\mathrm{erg\,s^{-1}}$. Pozorovanou hodnotu rentgenového zářivého výkonu se dosud nepodařilo konzistentně vysvětlit prostřednictvím žádného z modelů sekundární složky dvojhvězdy. V této práci se nejprve zaměřujeme na teorii o horkých podtrpaslících, hvězdných větrech a samotném binárním systému HD 49798/RX J0648.0–4418. Hlavní část této práce tvoří analýza UV spekter pořízených kosmickou observatoří IUE. Měříme parametry krátkovlnné složky spektrální čáry N V. Z těchto parametrů vypočítáme konečnou rychlost hvězdného větru z HD 49798 a předpovídáme rentgenový zářivý výkon. Určená konečná rychlost hvězdného větru dává v případě sekundární složky typu bílého trpaslíka rentgenový zářivý výkon, který je v souladu s pozorováním.

# Abstract

HD 49798 is the only known X-ray binary where the mass donor is a O-type hot subdwarf. Its companion is a compact object of yet unknown nature, either white dwarf or neutron star, with fast spin period $P = 13.2\,\mathrm{s}$ and steady spin up $\dot{P} = -2.28 \times 10^{-15}\,\mathrm{s\,s^{-1}}$. Due to stellar wind activity and the accretion, the binary exhibits a significant X-ray luminosity of $L_X \approx 10^{32}\,\mathrm{erg\,s^{-1}}$. The observed value of the X-ray luminosity has not yet been consistently explained by any model of the secondary component of a binary star. In this thesis, we firstly focus on the theory about hot subdwarfs, stellar winds and the binary system HD 49798/RX J0648.0–4418 itself. The main part of this thesis consists of analysis of UV spectra taken by space observatory IUE. We measure the parameters of the short wavelength component of N V spectral line. From these parameters we calculate terminal velocity of the stellar wind from HD 49798 and predict X-ray luminosity. The determined terminal velocity of the stellar wind, assuming white dwarf-type secondary component, gives an X-ray luminosity that is consistent with observations.

MUNI
SCI

MASARYKOVA UNIVERZITA
PŘÍRODOVĚDECKÁ FAKULTA
KOTLÁŘSKÁ 2, 611 37 BRNO
IČ: 00216224
DIČ: CZ00216224

# ZADÁNÍ BAKALÁŘSKÉ PRÁCE

Akademický rok: 2024/2025

| | |
|---|---|
| **Ústav:** | Ústav teoretické fyziky a astrofyziky |
| **Studentka:** | Petra Tereza Bukovinská |
| **Program:** | Fyzika |
| **Specializace:** | Astrofyzika |

Ředitel *ústavu* PřF MU Vám ve smyslu Studijního a zkušebního řádu MU určuje bakalářskou práci s názvem:

| | |
|---|---|
| **Název práce:** | Proměnnost ultrafialového spektra rentgenové dvojhvězdy HD 49798 |
| **Název práce anglicky:** | Ultraviolet spectral variability of X-ray binary HD 49798 |
| **Jazyk práce:** | angličtina |

**Oficiální zadání:**
Dvojhvězda HD 49798 je jediným známým zástupcem rentgenových dvojhvězd s hmotnou složkou, kde primárem je horký podtrpaslík. Předpokládá se, že rentgenové záření této dvojhvězdy vzniká v důsledku akrece hvězdného větru podtrpaslíka na kompaktní složku. Nepřímé důkazy ukazují na to, že kompaktní složkou v této dvojhvězdě je zřejmě bílý trpaslík. V takovém případě by ale byl předpokládaný rentgenový zářivý výkon podstatně nižší než ukazují pozorování. Možným řešením této nesrovnalosti je zpomalení hvězdného větru rentgenovým zářením. To by se projevilo orbitální proměnností ultrafialových profilů hvězdného větru. Cílem práce je studium fázové proměnnosti ultrafialových profilů typu P Cygni. Bude určena konečná rychlost větru v jednotlivých fázích a bude diskutováno, zda změna rychlosti větru může vysvětlit pozorovaný zářivý výkon. Také bude studována ultrafialová světelná křivka této dvojhvězdy.
Literatura


- Krtička, J.; Janík, J.; Krtičková, I.; Mereghetti, S.; Pintore, F.; Németh, P.; Kubát, J.; Vučković, M.: Hot subdwarf wind models with accurate abundances. I. Hydrogen dominated stars HD 49798 and BD+18 2647, 2019, Astronomy & Astrophysics, 631, A75, 11
- Krtička, J.; Kubát, J.; Krtičková, I.: Wind inhibition by X-ray irradiation in HMXBs: the influence of clumping and the final X-ray luminosity, 2018, Astronomy & Astrophysics, 620, A150
- Krtička, J.; Kubát, J.; Krtičková, I.: Stellar wind models of subluminous hot stars, Astronomy & Astrophysics, 593, A101


| | |
|---|---|
| **Vedoucí práce:** | prof. Mgr. Jiří Krtička, Ph.D. |
| **Datum zadání práce:** | 23. 10. 2024 |
| **V Brně dne:** | 10. 5. 2025 |

Zadání bylo schváleno prostřednictvím IS MU.

Petra Tereza Bukovinská, 13. 11. 2024
prof. Mgr. Jiří Krtička, Ph.D., 18. 11. 2024
RNDr. Luboš Poláček, 4. 12. 2024

# Poděkování

V první řadě bych chtěla poděkovat svému vedoucímu prof. Mgr. Krtičkovi Ph.D za neocenitelnou pomoc, trpělivost a odborné vedení při psaní této práce. Mé upřímné uznání a vděk patří také všem autorům publikací, z jejichž článků jsem při psaní čerpala. Nemohu opomenout ani svou rodinu a blízké, kteří mě během studia a při přípravě této práce vždy podporovali.

# Prohlášení

Prohlašuji, že jsem svoji bakalářskou práci vypracovala samostatně pod vedením vedoucího práce s využitím informačních zdrojů, které jsou v práci citovány.

Brno 13. 5. 2025

. . . . . .

Petra Tereza Bukovinská

# Contents

# Introduction

HD 49798 is a high mass X-ray binary that consists of hot O-type subdwarf and a compact companion of unknown nature [Heber, 2016]. It is the only known X-ray binary with a hot subdwarf that accretes matter onto a compact companion [Rigoselli et al., 2023]. Both the accretion and caused X-ray luminosity are likely the effects of stellar wind from the hot subdwarf.

The companion, RX J0648.0-4418, is curious star itself. It is compact with mass slightly above the solar mass and shows steady spin-up decrease about $2 \times 10^{-15}\,\mathrm{s\,s^{-1}}$ [Mereghetti et al., 2021]. Its nature is yet unknown, but it is highly possible that it is a young white dwarf which is still contracting [Popov et al., 2018]. This would make it the first observed young contracting white dwarf and help us better understand the evolution and characteristics of similar stars.

The first chapter is a brief overview of hot subdwarfs. The chapter discusses their characteristics and evolution processes, but does not omit information about their chemical composition and most importantly, hot subdwarfs in binaries.

Second chapter follows as another overview. This time about stellar wind of hot stars. It discusses radiatively driven winds in such stars, their mass loss and P Cygni profiles which appear in the spectra of HD 49798.

The subject of Chapter 3 is HD 49798 itself. The chapter offers information about the characteristics of this peculiar binary system, its problematics, possible theories of the nature of the compact companion, and previous results of calculation of X-ray luminosity.

These theoretical chapters are followed by the practical Chapter 4, which consists of data analysis of the spectra. In this chapter the short-wavelength component of N V doublet is fitted and the parameters are used to calculate the terminal velocity of the stellar wind from HD 49798. This leads to estimates of its X-ray luminosity $L_{\mathrm{X}}$ and comparison it to the observed lumonosity $L_{\mathrm{X\,obs}} \approx 10^{32}\,\mathrm{erg\,s^{-1}}$ [Rigoselli et al., 2023].

# Chapter 1

# Hot Subdwarfs

## 1.1 Introduction

Hot subluminous stars of spectral types O and B are mostly core helium burning objects that represent late stages of low-mass star evolution. They are positioned between main sequence and white dwarf sequence [Heber, 2016]. In the following chapters we will discuss properties of subdwarfs such as their chemical composition, evolutionary models and subdwarf binaries.

## 1.2 Evolution process

The main challenge for understanding the hot subdwarf formation is to explain the large mass lost prior to or at the start of core helium burning. However, it is important to note that not all hot subdwarfs are core helium burning objects as certain masses of some subdwarfs are too low to start the core helium burning [Heber et al., 2003]. In the following paragraphs we will dive into the most notable evolutionary models.

The core helium burning phase follows the red giant phase. Core helium burning subdwarfs can be found on the horizontal branch of the HR diagram as can be seen on figure 1.1. Stars with smaller less massive envelopes shift to bluer end [Heber, 2009, 2016]. In stars with initial mass $M \leq 2.3 M_{\odot}$ helium burning is ignited in the degenerate core. This leads to helium core flash. At this time, the core mass is fixed in a narrow range and depends slightly on metallicity and helium abundance [Sweigart, 1987]. The star gains higher temperature until it reaches the white dwarf cooling track. Its gravity increases and the star avoids an asymptotic giant branch [Heber, 2016].

### 1.2.1 Hot flasher

As mentioned above, one of the possible scenarios for stars with low mass is helium core flash. It may occur at the tip of the red giant branch. Or, if the star loses a lot of mass on the red giant (RG) branch, when the star is departing from the RG branch to the white dwarf cooling track [Castellani and Castellani, 1993].

There are three possible types of hot flashers based on evolutionary phase in which it occurs. The early one, later one with shallow mixing and the later one with deep mixing

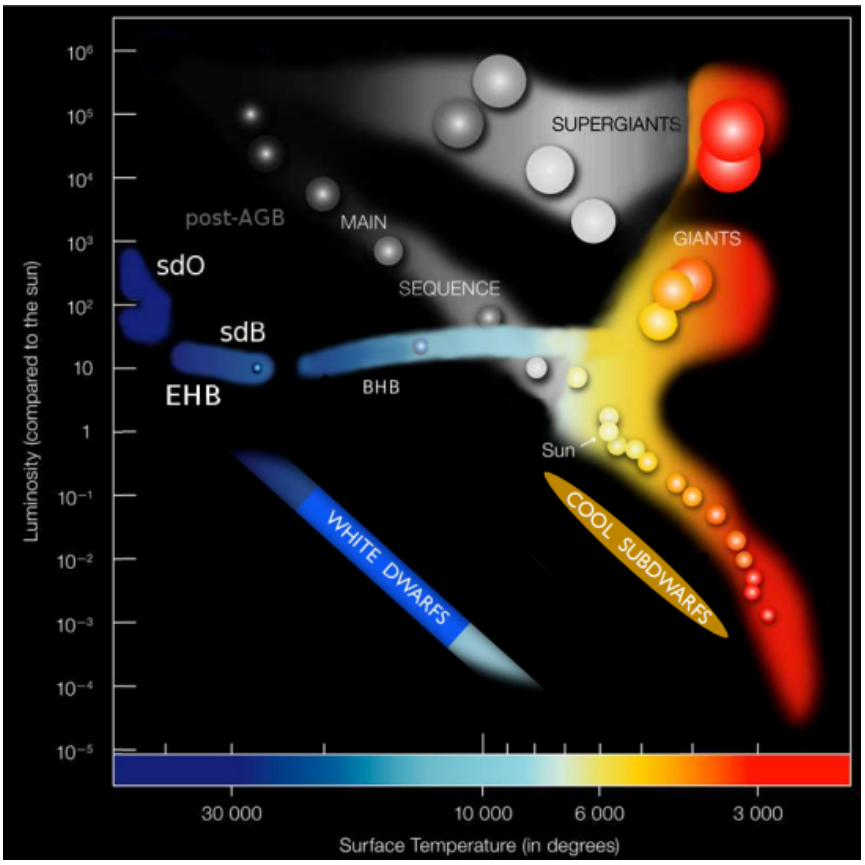


Figure 1.1: HR diagram; taken from [Heber, 2009]

[Miller Bertolami et al., 2008, Cassisi et al., 2003, Lanz et al., 2004].

First, let us look at the early hot flasher. In this case, the flash occurs early after star's departure from the red giant branch. The results are hot subdwarfs with standard H or He envelope.

As the name suggests, in the later hot flasher scenario, mixing occurs early on the stars move to the white dwarf cooling track. Thanks to the convective dilution of the envelope, the new subdwarf has atmosphere enriched with He and N.

In the later hot flasher model with deep mixing, first, the primary helium flash occurs, and the convective zone is created. After that, another flash ignites when the hydrogen envelope is engulfed in the convective zone. The resulting subdwarf is strongly enriched in He, C and N.

### 1.2.2 Helium mixing

[Sweigart, 1997a,b] researched another of the possible models - that is helium mixing on the red giant branch. In this case, the outer convective envelope can extend into the hydrogen-burning shell, causing some helium to mix into the envelope. If helium mixing occurs, the luminosity of the RG branch tip increases and large amount of mass is lost.

[Sweigart, 1997b] believes that the mixing can be caused by rapid rotation and [Tailo et al., 2015] suggests that rapid rotation is a result from star forming history and early dynamics of massive globular clusters.

### 1.2.3 Binary evolution

Many hot subdwarfs can be found in close binaries. This suggests that they were possibly formed by binary interactions. Among the possible processes are common envelope evolution (CE) [Paczynski, 1976], Roche lobe overflow (RLOF) and white dwarf merger [Webbink, 1984]. In this section, we will take a closer look at each of these processes.

Firstly, we need to discuss how common envelope is formed. The hot subdwarf progeny typically fills Roche's lobe when it is close to the tip of red giant branch. Now, the mass transfer rate plays important role. If it is not high enough, the companion can't accrete all the matter and the common envelope is formed. Then the friction with the gas causes the two components to spiral until the common envelope gains enough orbital energy to be ejected. This process results in a red giant core which will become the subdwarf and its unchanged companion. If the companion is the main sequence star then later, when the star becomes red giant, it will fill Roche lobe and the common envelope is ejected again, leaving the B-type subdwarf (sdB) + white dwarf (WD) binary [Heber, 2016].

In the RLOF scenario, there is no common envelope formed due to dynamically stable mass transfer which allows the companion to accrete the matter. The red giant loses its entire envelope in this process and becomes a subdwarf. The result is long period sdB + main sequence star binary with periods from 10 to 500 days [Han et al., 2003].

Another possibility is formation of a binary with two subdwarfs, when the envelope of two giant stars is ejected. Possible example of such double core common envelope evolution may be He-sdB PG 1544+488 [Şener and Jeffery, 2014, Justham et al., 2011].

[Ivanova et al., 2013] discovered that about a fifth of all planetary nebulae are formed from ejected common envelope. Few of them may be post RG branch objects, however Hall et al. argued that there is an uncertainty of identifying the suggested planetary nebulae as post RG branch system [Hall et al., 2013]. Common envelope nebula is visible only for a short period of time – a few ten thousand years, thus we need to inspect a lot of sdB stars to discover a post RG branch nebulae associated with sdB star.

### 1.2.4 White dwarf merging

The last but not least process mentioned is helium white dwarf merging [Webbink, 1984]. [Zhang and Jeffery, 2012] proposed three possible processes of merging two He white dwarfs. This could be the plausible explanation of the formation of single hot subdwarfs.

The first is the slow merger model. The larger, less massive, white dwarf fills the Roche lobe, and its entire mass is transferred to form a disk. The material then slowly accretes to its companion.

In a different scenario the mass of the less massive white dwarf can directly fall onto the primary, more massive, white dwarf surface. The temperature of the material is about $10^8$K and it can form corona in just a few minutes.

The composite merger model is based on the results of 3D hydro simulations by [Lorén-Aguilar et al., 2009]. As the name suggests, it combines both previously discussed merger models. Part of the mass forms a hot corona while the other forms a cold disc.

Even though the merger of two white dwarfs seems like a possible explanation for existence of single subdwarfs, the observed mass distribution is narrower than the predicted one by the models. [Soker, 1998, Politano et al., 2008] suggested an alternative. Single subdwarfs may be formed by merging of a red-giant core and a low mass star or a brown dwarf. [Politano et al., 2008] believes that this process would form rapidly rotating horizontal branch stars, of which some may be of sdB type.

Another suggestion, by [Clausen and Wade, 2011] is that the coalescence of helium white dwarf with a low mass hydrogen burning star would create a star with a helium core and thick hydrogen envelope that evolves into sdB star. This could also explain sdBs' slow rotation rates.

However, we shouldn't forget that it is also possible, that the apparent single sdB stars have companions yet undetected.

## 1.3 Chemical composition

Hot subdwarfs often have peculiar spectra, therefore additional spectral classes are needed. They are divided based on the spectral class into sdB, sdOB and sdO types, plus their counterparts - He-sdB and He-sdO [Heber, 2016].

### 1.3.1 sdB stars

Helium abundance is an important parameter for subdwarfs. The amount of helium seems to correlate with effective temperatures as it was observed to increase with rising temperatures [Edelmann et al., 2003].

Abundances of other elements have also been measured. Results from the ESO/SPY's optical spectroscopy [Heber et al., 2000, Heber and Edelmann, 2004, Napiwotzki et al., 2001, Edelmann et al., 2001, 2006, 1999], show that nitrogen abundances tend to be slightly subsolar, and oxygen is also depleted and shows slight scatter. Magnesium and iron abundances almost attain solar. Carbon varies from star to star, scattering from strongly subsolar to slightly supersolar.

Silicone, aluminum, and sulfur are depleted, with Si showing a large scatter. Heavier elements, from potassium to cobalt, are enriched. Titanium was found in half of the observed stars and vanadium in one third. Few stars have scandium and chromium present. All these heavier elements are enriched.

Spectral analysis of UV spectra offers similar results. All elements beyond silver show enrichment in observed stars. The only exception is Fe. However, analysis of UV spectra is available only for a few hot subdwarfs.

### 1.3.2 sdO stars

In this section we will discuss the composition of O-type subdwarfs. Even though O-type subdwarfs are sdBs' "neighbours" on the HR diagram, they are different in both the chemical composition and evolutionary status.

Most hydrogen rich sdO stars are progeny of normal sdB stars. Core helium burning had stopped and left C/O core with helium burning in the shell.

Out of helium poor sdO stars, a few have been studied carefully using far UV -spectra taken with FUSE satellite for example Feige 110, AA Dor and EC 11481-2303 [Klepp and Rauch, 2011, Rauch et al., 2010, 2014].

Similar to the composition of sdB stars, lighter elements tend to be subsolar to solar. However, Feige 110 is an exception with strongly depleted C, O and Si. Iron in EC 11481-2303 is strongly enriched, while solar in other two stars.

Abundances and chemical composition of He-sdO stars were determined using the data from the ESO/SPY. Among the observed sample, He abundances show only slight scatter. Carbon is either slightly super-solar or strongly depleted, and nitrogen is super-solar for most of the stars. However, there are stars in the sample with strongly depleted nitrogen [Hirsch and Heber, 2009].

## 1.4 Binary systems and methods of their detection

As it was stated before, many subdwarfs can be found in close binaries. Among their companions there are white dwarfs, brown dwarfs or low-mass main sequence stars. Binaries with neutron stars or black holes are predicted. One of the possible methods of subdwarf binary detection includes measuring radial velocity variability, which is particularly effective for finding short period sdB + white dwarf and sdB + dM systems. With the help of Palomar Green catalog [Green et al., 1986, Saffer et al., 1998] and [Moran et al., 1999] discovered seven sdB + white dwarf binaries with periods from 0.25 to 2.5 days. Thanks to the efforts of [Maxted et al., 2001, Morales-Rueda et al., 2003, Napiwotzki et al., 2004], as well as other surveys, mainly ESO/SPY and SDSS, the number of detected subdwarf binaries has quickly risen.

All the mentioned short period binaries are single lined and have unseen companion, possibly a low mass star, brown dwarf or a white dwarf. Therefore, properties of the companion have to be discovered by other methods, with photometry being one of the most important. By observing the reflection effect on the companion, or the lack of, it is possible to distinguish low-mass star and brown dwarf companions, on which reflection effect is significant, from white dwarfs [Maxted et al., 2002, 2004, Shimanskii et al., 2008]. Eclipsing systems (for which the companion mass can be calculated) make about 10% of the sample. Therefore, the mass of the companions in other systems has to be derived using mass function adopting the canonical mass for sdB stars [Kupfer et al., 2015, Kawka et al., 2015]. The mass of objects is also an important parameter for discovering the nature of the companion. If it is higher than $0.45 M_{\odot}$, it excludes main-sequence star companions, as they would be detectable in the optical spectra [Lisker et al., 2005].

## 1.5 X-rays from O-type stars

Due to the stellar winds, O-type stars emit X-rays [Lucy and White, 1980, Owocki et al., 1988] with X-ray luminosities $L_X = 10^{-7} L_{bol}$ [Antokhin et al., 2008]. Despite that, their mass loss is often too low for them to be expected X-ray sources, with HD 49798, the subject of this thesis, being a curious exception [Heber, 2016]. Though it is important to note, that the X-ray luminosity doesn't come from the HD 49798 itself, but rather than its companion on which it accretes matter. Indeed, accretion onto companion is one of the two ways that can produce X-rays in hot subdwarfs with the other being wind emission [Mereghetti and La Palombara, 2016]. In some cases, even both can occur. This allow us to discover subdwarf binaries with neutron star or a white dwarf, which under other circumstances would be troublesome to detect. If that is the case, the expected X-ray luminosity can be calculated as:

$$L_X = \frac{G M_X}{R_X} \dot{M}_A \sim \frac{G M_X}{R_X} \left( \frac{R_A}{2a} \right)^2 \dot{M}_W, \tag{1.1}$$

where $M_X$ is mass of the compact companion, $R_X$ its radius and $\dot{M}_A$ mass accretion rate. After further rearranging of the equation, $a$ corresponds to the orbital separation and $\dot{M}_W$ wind mass loss rate from the subdwarf.

$$R_A = \frac{2GM_X}{v_w^2 + v_{orb}^2}, \tag{1.2}$$

where $v_{orb}$ is the orbital velocity and $v_w$ is the wind velocity [Mereghetti and La Palombara, 2016].

There are two velocity laws suggested by [Hatchett and McCray, 1977]. The first one, where wind velocity is constant, and the second one is described by the beta law, further discussed in the following chapter.

# Chapter 2

# Hot star winds

As was stated in previous section, HD 49798 is unique thanks to its stellar wind. In this chapter I will look into the general information about this phenomenon and methods of detecing its parameters.

Stellar wind is outflow of plasma from different types of stars. It can often be discovered by detecting P Cygni lines, which consist of an absorption line in the blue region and emission line in the red region. P Cygni lines are often wide, with velocity, caluclated from Doppler shift, much higher than star's escape velocity [Krtička, 2015]. Due to stellar wind activity, stars can lose their mass. The mass loss rate varies from star to star. For Sun-like stars the expected mass loss is $10^{-14}\,M_\odot\,yr^{-1}$. The mass loss gets much higher for more massive stars, reaching $10^{-7}-10^{-5}M_\odot\,yr^{-1}$ for massive O type stars [Vink, 2024].

However, one is wrong to assume that low-mass star evolution isn't affected by mass loss. In fact, during RG branch phase the mass loss rate can reach $\sim 10^{-6}\,M_\odot\,yr^{-1}$ and even $10^{-4}\,M_\odot\,yr^{-1}$ at the top of the asymptotic giant branch (AGB) [Höfner and Olofsson, 2018].

The mass loss rate can be expressed as:

$$\dot{M} = 4\pi r^2 \rho(r) v(r), \tag{2.1}$$

where $\rho$ is wind density and $v$ is wind velocity. The momentum of stellar wind has to overcome star's gravitation, therefore we can write equation:

$$v\left(\frac{dv}{dr}\right) = -\frac{GM}{r^2} + C\left(\frac{dv}{dr}\right)^{\alpha}_{Sob}, \tag{2.2}$$

where C is a constant [Castor et al., 1975]. We predict that wind velocity behaves as beta law. Therefore:

$$v(r) = v_\infty\left(1 - \frac{R_*}{r}\right)^{\beta}, \tag{2.3}$$

where $R_*$ is the radius of the star, $v_\infty$ wind terminal velocity and $\beta$ typically 0.5. The mass loss rate scales both with the luminosity of the star and the Eddington factor $\Gamma$.

$$\Gamma = \frac{a_{\rm rad}}{a_{\rm g}} = \frac{\frac{\sigma_{\rm Th}}{\mu_{\rm e}} L_*}{4\pi G M_* c}, \tag{2.4}$$

where $a_{\mathrm{rad}}$ is radiative acceleration due to free electrons, $a_{\mathrm{g}}$ gravitational acceleration of the star, $\sigma_{\mathrm{Th}}$ effective cross-section of Thomson scattering with $\sigma_{\mathrm{Th}} = 6.65 \times 10^{-24}\,\mathrm{cm}^{-2}$, and $\mu_e$ is the ratio of density $\rho$ and number of free electrons.

## 2.1 Radiatively driven wind

In hot stars, stellar wind is driven by the radiative force from the light absorption in the lines of heavier elements [Castor et al., 1975, Puls et al., 2008]. Therefore, stellar wind properties are largely influenced by the metallically and luminosity of a star. For O-type stars with mass above $25\mathrm{M}_{\odot}$ there are uncertainties of a factor 2-3 in mass loss rates due to wind clumping, radiative transfer treatment in subsonic regions, and wind hydrodynamics [Mereghetti et al., 2013, Rauch et al., 2014, Mereghetti et al., 2021].

### 2.1.1 CAK

The Castor-Abbot-Klein theory [Castor et al., 1975] describes the radiative force in terms of force multiplier. The radiative force depends on the opacity from Doppler shifted lines – therefore larger the opacity means larger the radiative force.

The main problem that may arise when using the Castor-Abott-Klein theory is that it uses the Sobolev approximation, which may lead to inprecise results.

### 2.1.2 Monte Carlo

The most used method is the Monte Carlo method [Vink, 2000, Abbott and Lucy, 1985]. With this method, the photon packets are tracked as they travel from to photosphere to the outer wind. Meanwhile, momentum and energy of photons are transferred to the gas particles. This method of modeling is great for both relatively weak winds and for O-type stellar winds.
The mass loss rate relation can be aproximated as:

$$\dot{M} \propto L_*^{2.2} M_*^{-1.3} T_{\mathrm{eff}} \left( \frac{v_\infty}{v_{\mathrm{esc}}} \right)^{-1.3}, \tag{2.5}$$

and it further can be simplified to

$$\dot{M} \propto L_*^{1.6}. \tag{2.6}$$

However it is important to know that these relations work only for winds with $\Gamma < 0.5$. Stars that do not fulfill this criteria are for example: stars with high initial mass and luminosity, less extremely luminous stars that have approached Eddington's limit by their evolution.

### 2.1.3 Comoving frame method

Another method, great for supersonic stellar wind, is the comoving frame method. Within this method, the radiative transfer equation is solved as partial differential equation. In this case, the radiative acceleration is given by:

$$a_{rad} = \frac{1}{c} \int \kappa_\nu F_\nu d\nu, \tag{2.7}$$

where $\kappa_\nu$ is the frequency dependant on the opacity and $F_\nu$ is the flux [Vink, 2022].

## 2.2 Mass loss rate

Radiative driven wind theory can predict the terminal velocity and mass loss rate. The first quantity can be directly observed from P Cygni absorption profiles, as the maximum speed of the wind can be calculated from the Doppler's shift at maximum line width, and the latter can be derived from the wind density and the equation of continuity [Hillier, 1991, Krtička, 2015]

There are several methods of determining mass loss rate. Other then previously mentioned P Cygni line the methods include multiwavelength diagnostic - getting the mass loss rate is from stellar continua at long wavelengths or spectral line transitions in the optical or UV regions, H$\alpha$ recombination emission lines, X ray method or bow shock method [Vink, 2022]]. I will briefly describe the methods most useful for O-type stars.

One of such common ways to derive $\dot{M}$ for O-type stars is using the H$\alpha$ recombination lines [Klein and Castor, 1978, Drew, 1989, Lamers and Leitherer, 1993, Puls et al., 1996]. The advantage of using this method is that the porosity effects can be neglected due to H$\alpha$ being optically thin in the main part of the emitting wind. However, this method also has disadvantages such as it is not sensitive to mass loss rates below $10^{-7} M_\odot \mathrm{yr}^{-1}$ [Mokiem et al., 2007], therefore another method needs to be used in such cases. It is also important to note that stellar winds are time dependent and that might cause inhomogeneities – the "wind clumping" [Hamann et al., 2008, Puls et al., 2008]. This method is quite sensitive to wind clumping, therefore it is crucial not to neglect it, otherwise it might provide incorrect results.

### 2.2.1 Wind clumping

The wind clumping occurs in O-type stars at about half the terminal velocity and at about 1.5 stellar radii. We can differentiate optically thin clumping – microclumping and optically thick clumping – macroclumping. When looking at microclumping we assume that the wind consists of many smaller wind clumps with void in between them [Owocki, 2015]. In the optically thick clump photons may interact with the gas several times before being able to escape. The optical thickness depends on the abundance, ionization fraction, and cross section of the transition.

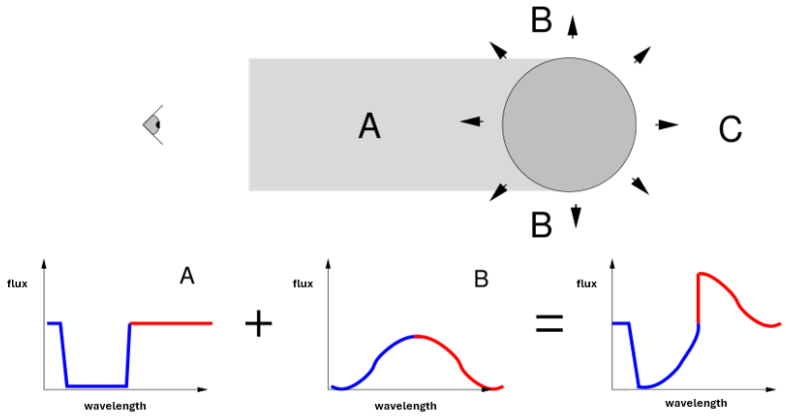


Figure 2.1: Formation of P Cygni profile [Krtička, 2015]

## 2.3 Stellar evolution and mass loss

Mass loss might affect stellar evolution. It has the largest effect for very massive stars, but even less massive stars can lose great amount of their mass throughout their evolution. Stars lose their mass during all phases of their life, but the mass rate might differ in each phase [Vink, 2022]. Stellar winds don't only cause mass loss but might also affect star's rotational evolution. Likewise, the rotation might affect wind strength and latitudinal dependence.

## 2.4 P Cygni profiles

P Cygni profiles have blue shifted absorption component and red shifted emission component due to the stellar wind. They are most prominent in the spectral lines C IV, Si IV and N V, which will be used in this thesis, of O type stars. Even though the mass loss is small, the Doppler shift is clear in the spectra which makes it a great indicator of mass loss and stellar wind activity [Lamers, 1999].

Figure 2.1 shows the formation of P Cygni profiles [Krtička, 2015]. The gas in grey rectangle A is moving towards the observer. Without the stellar wind, the observer would detect only photons from that area. However, for stars with stellar wind, some of the photons from area A are scattered away and will not be detected. This causes the blue shifted absorption. Similarly, photons from area B are scattered all around and might be detected, causing the red shifted emission. Together, they form the P Cygni profile [Lamers, 1999]. The Doppler-shift of a blue edge of P Cygni line profile corresponds to the wind terminal velocity.

# Chapter 3

# HD 49798

## 3.1 HD 49798

The subject of this thesis, HD 49798, is a hot O-subdwarf located at $\alpha = 6\,\mathrm{h}\,48\,\mathrm{m}\,0.470\,\mathrm{s}$, $\delta = -44°\,18'\,58.43''$, J2000 [Thackeray, 1970]. Together with its compact companion RXJ0648.0-4418 of yet unknown nature, it forms the only known X-ray binary with a hot subdwarf [Heber, 2016].

## 3.2 Stellar parameters of HD 49798

HD 49798 has radius $R_{\mathrm{HD}} = 1.5 \pm 0.06\,\mathrm{R}_{\odot}$ [Krtička et al., 2019] and mass $M_{\mathrm{HD}} = 1.5 \pm 0.05\,M_{\odot}$ [Mereghetti et al., 2009] and orbital period $1.547666(6)$ d[Rigoselli et al., 2023]. It also has peculiar chemical composition, which needs to be taken into consideration when calculating mass loss rate. Carbon and oxygen are depleted, while nitrogen, nickel and iron are slightly supersolar [Krtička et al., 2019, Asplund et al., 2009]. Such composition is likely a results of its evolution [Krtička et al., 2019].

## 3.3 RXJ0648.0-4418

RXJ0648.0-4418 is a compact object with mass $M_{\mathrm{X}} = 1.22 \pm 0.05\,M_{\odot}$ [Rigoselli et al., 2023] and spin period P = 13.2 s [Kudritzki and Simon, 1978, Israel et al., 1997, Mereghetti et al., 2011]. The companion is most likely a white dwarf. However, a neutron star has also been considered. This claim supports observations of X-ray emission from the companion. Due to the mass of $1.22M_{\odot}$, it is difficult to distinguish these possibilities, therefore other methods must be used to discover its nature.

### 3.3.1 Luminosity and the nature of the companion

The expected luminosity for accretion onto the surface was calculated for both scenarios. According to [Rigoselli et al., 2023], the expected luminosity of neutron star with 12 km

radius would be:

$$L_x^{NS} \simeq 3 \times 10^{33} \left( \frac{\dot{M}_w}{2 \times 10^{-9} M_\odot} \mathrm{yr}^{-1} \right) \left( \frac{v_w}{1500\,\mathrm{km\,s^{-1}}} \right)^{-4} \mathrm{erg\,s^{-1}}, \tag{3.1}$$

where $\dot{M}_w$ is a mass loss due to the stellar wind and $v_w$ is the wind velocity. For the white dwarf companion with $R_{WD} = 3582\,\mathrm{km}$ [Nauenberg, 1972] the luminosity was calculated as $L_x^{WD} = 10^{31}\mathrm{erg\,s^{-1}}$ [Rigoselli et al., 2023]. Both of these values significantly differ from the observed one $L_x = 10^{32}\mathrm{erg\,s^{-1}}$[Mereghetti et al., 2016] with $L_x^{WD}$ being lower by an order and $L_x^{NS}$ higher.

Despite the differences in orders in both cases, there are reasonable explanations. The effects related to the rotating magnetosphere may greatly decrease the accretion flow reaching the surface of a neutron star. Under these circumstances, it is possible to expect luminosity such as the observed one [Rigoselli et al., 2023].

In the second case, white dwarf, the notable effect is dependency of the accretion rate on the wind velocity. With the reduction of wind velocity, the luminosity can be increased to the observed one. [Krtička et al., 2019] suggested that the decrease in wind velocity may be caused by X-ray photoionization.

### 3.3.2 Young contracting white dwarf theory

Popov et al. is in favour of the white dwarf theory and further proposes that the companion is a young white dwarf which is still contracting [Popov et al., 2018]. They support this claim by the agreement of their constructed cooling curve with the observed luminosity. The contraction would also explain its spin up. However, [Popov et al., 2018] also points out that, in the future, the spin evolution of the white dwarf will be more influenced by the angular momentum gained through accretion rather than the contraction [Popov et al., 2018].

### 3.3.3 Thermal component and the nature of the companion

Another claim that supports the white dwarf theory are the observations of the X-ray flux emitted in a soft and strongly pulsed thermal component, which could be represented with a blackbody of radius $R \sim 30\,\mathrm{km}$ and temperature $kT \sim 30\,\mathrm{eV}$ [Mereghetti et al., 2011]. Those results could be expected of a hotspot on a white dwarf but would be too large for a neutron star [Mereghetti et al., 2021]. If the companion is indeed a white dwarf, it is a possible supernova Ia [Liu et al., 2010] or neutron star [Brooks et al., 2017] progenitor.

## 3.4 Spin up

RXJ0648.0-4418 shows a steady long-term spin period decrease at rate $\dot{P} = -2.15 \times 10^{-15}\,\mathrm{s\,s^{-1}}$ [Mereghetti et al., 2016]. Explaining this by accretion torques is challenging, but Popov et al. suggest another solution unrelated to the accretion - the aforementioned contracting white dwarf. According to their calculations, a white dwarf with mass $M_\mathrm{X} = 1.28\,\mathrm{M}_\odot$ and 2 Myr old could indeed have spin up rate $\dot{P} = -2.15 \times 10^{-15}\,\mathrm{s\,s^{-1}}$ as

it is observed with RXJ0648.0-4418 [Popov et al., 2018]. They also point out that this would be the first observational evidence of a young contracting white dwarf.

## 3.5 X-ray emission

Observations from 2018 confirmed that the X-ray emission is significant even during the eclipse, when the compact object is completely occulted [Mereghetti et al., 2021]. This might be emission from the stellar wind itself or the emission form the compact object is scattered in the wind. These results are consistent with previous observations [Mereghetti et al., 2009, 2013]. Fits for 2014 and 2020 spectra gave close values for the blackbody component but different values for the power law, meaning lower flux in 2020. This indicates long-term variability in the hard X-ray component and supports previously made light curves. All other parameters remained consistent with previous observations [Mereghetti et al., 2021, 2016]. Mereghetti et al. believes that the HD 49798 might show changes in the mass accretion rate due to possible time-variable inhomogeneities in its stellar wind [Mereghetti et al., 2021].

# Chapter 4

# Data analysis

## 4.1 Used data

The data used for this thesis were downloaded from archive INES through SPLAT-VO[1]. All examined spectra were taken by space observatory IUE with SWP camera with spectral resolution 0.2 Å and high dispersion. The spectra spanned from 1150 Å to 1980 Å, allowing us to see the whole P Cygni profile from which the stellar wind velocity was determined. Table 4.1 shows downloaded spectra and modified heliocentric Julian date of mid-exposure, therefore number of days since midnight of 17.11.1858 [2].

| **Data** | **Time** | **Phase** |
|---|---|---|
| - | [MJD] | - |
| swp01336HS.fits | 43607.41328 | 0.142502 |
| swp01698HS.fits | 43661.95311 | 0.382683 |
| swp01699HS.fits | 43662.02426 | 0.428527 |
| swp02513HS.fits | 43758.37501 | 0.684046 |
| swp04024HS.fits | 43898.02316 | 0.915497 |
| swp04767HS.fits | 43595.6617 | 0.549404 |
| swp04768HS.fits | 43959.69478 | 0.763643 |
| swp04773HS.fits | 43959.85333 | 0.866087 |
| swp04776HS.fits | 43959.95859 | 0.934100 |
| swp04779HS.fits | 43960.03081 | 0.980763 |
| swp04798HS.fits | 43961.8873 | 0.180305 |
| swp04802HS.fits | 43961.99921 | 0.252614 |
| swp05478HS.fits | 44034.70434 | 0.229888 |
| swp05481HS.fits | 44034.83147 | 0.3120311 |

Table 4.1: Spectra used for calculating stellar wind velocity

[1]Downloaded from: https://www.g-vo.org/pmwiki/About/SPLAT
[2]Taken from: https://core2.gsfc.nasa.gov/time/

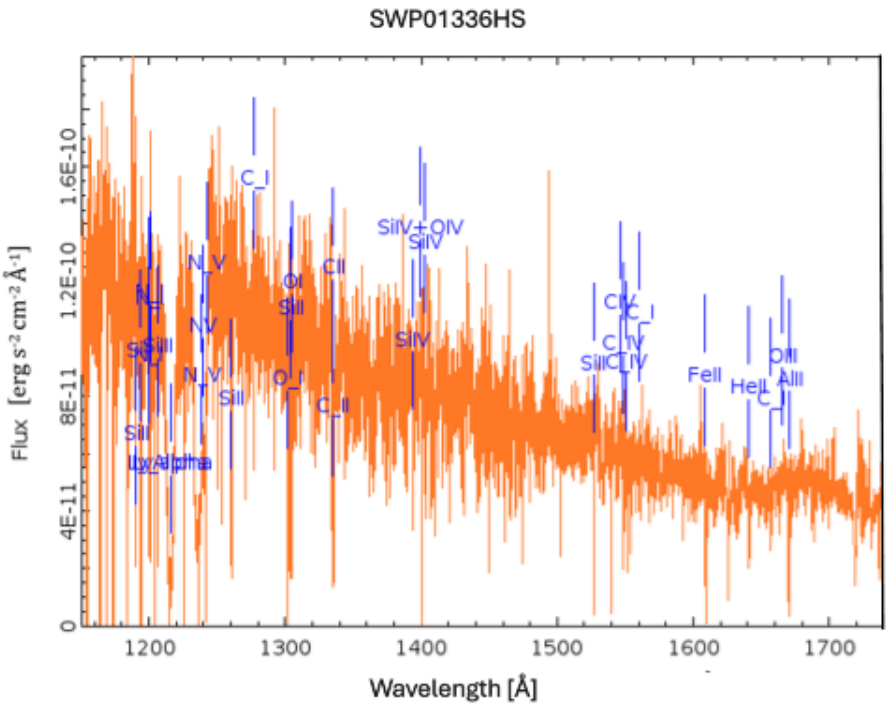


Figure 4.1: Identified spectral lines

## 4.2 Data processing

### 4.2.1 Spectra

Spectra from data file swp01336HS.fits were taken to identify the most prominent spectral lines. Figure 4.1 shows the line identification from SPLAT-VO.

In addition to the N V doublet, which is crucial for this thesis, the spectra also possesses other lines, such as C II, Si or O VI lines.

### 4.2.2 Gaussian fit

All used data were processed using Python code which is included in the appendix. Firstly, the spectra were limited to small interval of wavelengths - approximately from 1210 Å to 1275 Å. After plotting flux over wavelength, a prominent N V spectral line doublet has been identified in all spectra. However, only the component with shorter wavelength was used and its left slope of was fitted with Gaussian function:

$$y = y0 - A\exp\left(\frac{-(x-B)^2}{4C^2}\right). \tag{4.1}$$

In the Gaussian function, $y$ represents flux, and $x$ the wavelength, while $y0$, $A$, $B$, and $C$ are required parameters for the fit. Parameters are further described in table 4.2 and figure 4.2 shows examples of fitting. All figures of fits can be found in the appendix.

The fit required initial guesses of the parameters which were given as:

| parameter | description |
|---|---|
| y0 | value of continuum |
| A | amplitude (flux) |
| B | shifted wavelength |
| C | standard deviation of the Gaussian |

Table 4.2: Parameters of the Gaussian fit

```
initial_y0 = np.mean(ydata)
initial_B = xdata[np.argmin(ydata)]
initial_C = (np.max(xdata) - np.min(xdata)) / 4
initial_A = np.max(ydata) - initial_y0
```

Using the code, exact parameters of the Gaussian fit were given for each spectra.

| **Data** | **y0** | A | **B** | **C** | phase |
|---|---|---|---|---|---|
| - | $10^{-11}\,\mathrm{erg\,s^{-1}\,cm^{-2}\,\AA^{-1}}$ | $10^{-11}\,\mathrm{erg\,s^{-1}\,cm^{-2}\,\AA^{-1}}$ | Å | Å | |
| swp01336HS | 11.3(3) | 8.8(3) | 1234.99(5) | 1.22(6) | 0.142502 |
| swp01698HS | 7.6(1) | 5.6(1) | 1235.06(4) | 0.92(4) | 0.382683 |
| swp01699HS | 9.8(1) | 8.0(2) | 1234.98(4) | 0.94(4) | 0.428527 |
| swp02513HS | 10.7(2) | 8.7 (3) | 1234.49(6) | 1.14(6) | 0.684046 |
| swp04024HS | 9.5(2) | 7.0(2) | 1234.71(7) | 1.34(7) | 0.915497 |
| swp04767HS | 8.8(2) | 6.6(2) | 1234.62(8) | 1.25(8) | 0.549404 |
| swp04768HS | 8.9(2) | 6.6(2) | 1234.67(8) | 1.22(8) | 0.763643 |
| swp04773HS | 9.8(2) | 7.4(3) | 1234.81(9) | 1.36(9) | 0.866087 |
| swp04776HS | 10.8(3) | 8.3(3) | 1234.69(8) | 1.39(8) | 0.934100 |
| swp04779HS | 9.3(2) | 7.1(2) | 1234.62(7) | 1.20(7) | 0.980763 |
| swp04798HS | 10.2(4) | 7.3(4) | 1235.37(14) | 1.36(14) | 0.180305 |
| swp04802HS | 11.3(3) | 8.3(3) | 1235.08(7) | 1.09(7) | 0.252614 |
| swp05478HS | 9.5(2) | 6.7(3) | 1235.05(10) | 1.03(8) | 0.229888 |
| swp05481HS | 10.7(3) | 8.0(3) | 1235.12(10) | 1.12(9) | 0.3120311 |
| Average | 9.9(2) | 7.4(3) | 1234.88(8) | 1.19(8) | - |

Table 4.3: Parameters from fit.

### 4.2.3 Phase dependance of the Gaussian parameters

Derived data was plotted in phase diagrams on figure 4.3 using orbital period $P_{\mathrm{orb}} = 1.547666(6)\,\mathrm{d}$ and $\mathit{phase} = 0$ at $t = 54597.169$ MJD [Mereghetti et al., 2009]. The vertical bars in the phase diagram and the numbers in parenthesis in the table represent uncertainties of the parameters determined with the code. Total uncertainties for mean values were calculated using uncertanties for individual values and standard deviation of values for the parameter.

Values of parameter $y_0$ are scattered all around with no obvious phase dependance. Phases were chosen in a way that eclipse happens at $\mathit{phase} = 0$. The average value is $(\overline{y_0} = 9.9 \pm 0.2)\,10^{-11}\,\mathrm{erg\,s^{-1}\,cm^{-2}\,\AA^{-1}}$. Similarly, parameter A, the amplitude, is scattered evenly with average value of $(\overline{A} = 7.4 \pm 0.3)\,10^{-11}\,\mathrm{erg\,s^{-1}\,cm^{-2}\,\AA^{-1}}$. Phase dependence of parameter B is more visible. At the beginning of orbital phase, the parameter B is scattered around 1235.0 Å, with uncertainties around centesimals Å, occasionally reaching 0.1 Å. After $\mathit{phase} = 0.5$, the values of the parameter B drop below the average value $\overline{B} = 1234.88$ Å. The standard deviation of the Gaussian has higher values, between 1.2 Å

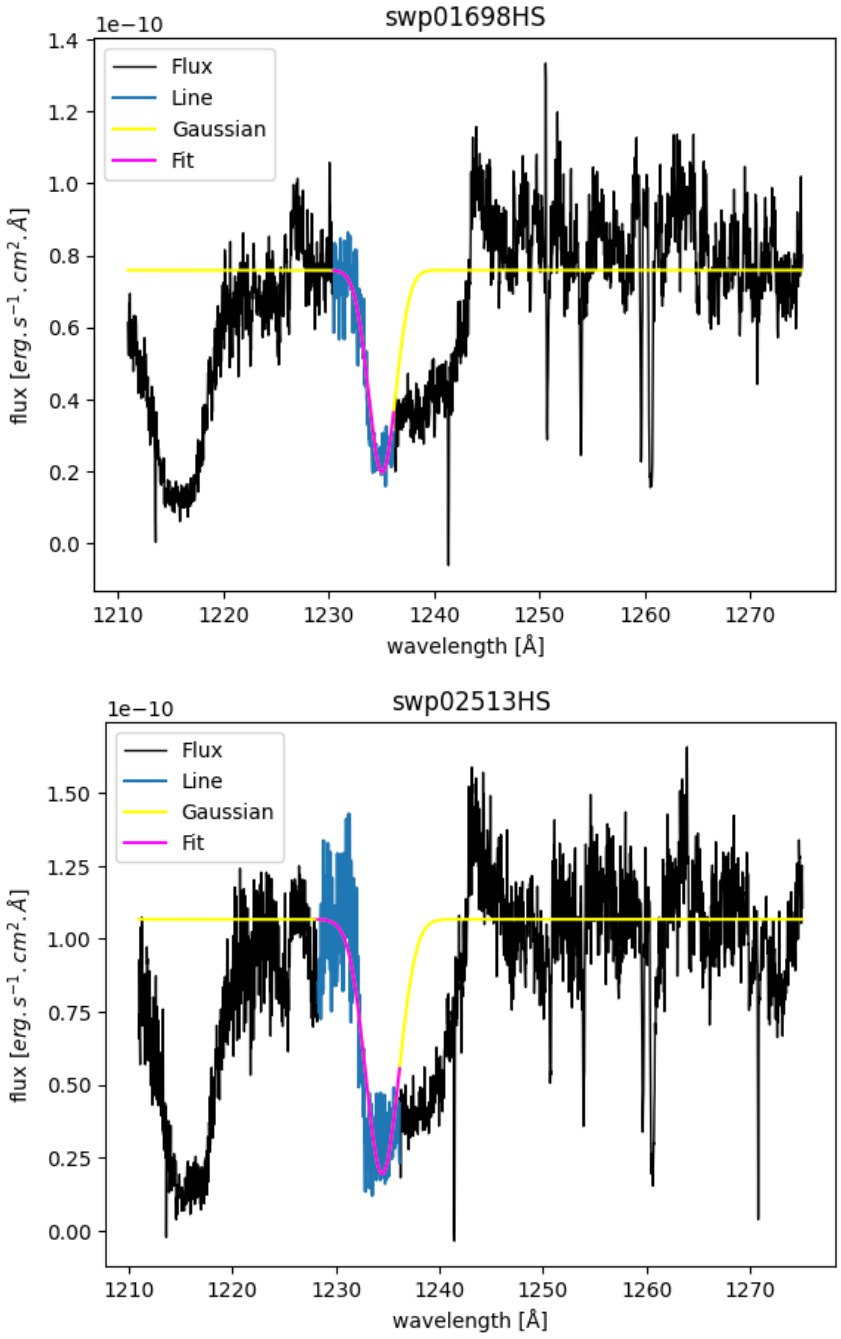


Figure 4.2: Example of fitting the data with Gaussian

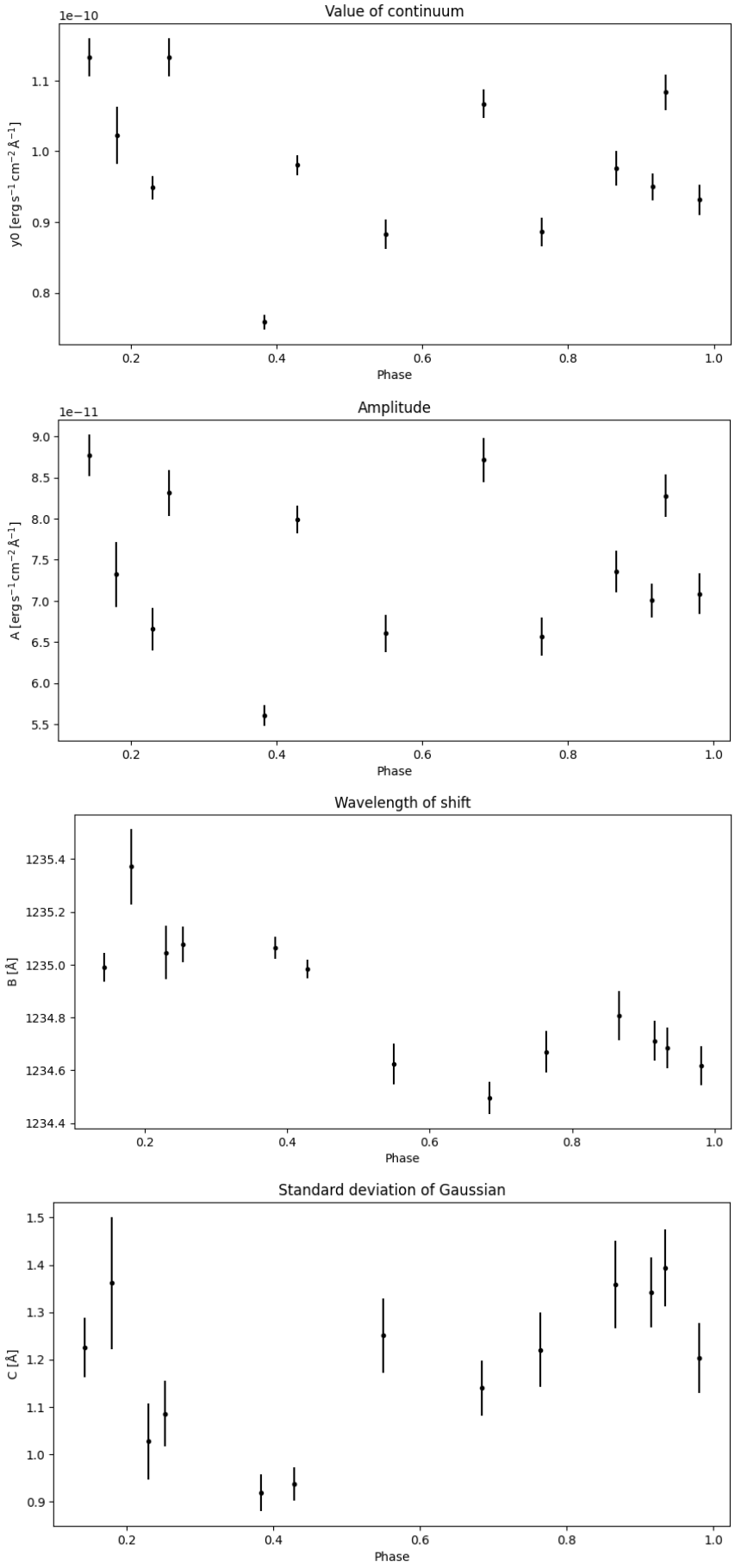


Figure 4.3: Phase diagrams of parameters

and 1.4 Å at the beginning of the phase. Parameter C then seems to drop in value and from $phase = 0.5$ rises again. However, with this parameter, it is likely that the seeming phase dependence is purely coincidental. More data is needed to prove or refute the phase variability of this parameter. Therefore, it would be wise to construct the phase diagrams once again, once more measurements are acquired.

### 4.2.4 Calculation of velocity

In order to determine the stellar wind velocity, a radial velocity was needed. Assuming both stars orbit circularly around the common center of mass, it is possible to calculate the orbital velocity of the subdwarf as:

$$v_{\mathrm{HD}} = \frac{M_{\mathrm{X}}}{M_{\mathrm{HD}}} v_{\mathrm{X}}. \tag{4.2}$$

Masses $M_{\mathrm{X}}$ and $M_{HD}$ were considered as $M_{\mathrm{X}} = 1.22\,\mathrm{M}_{\odot}$ for the compact object, and $M_{\mathrm{HD}} = 1.41\,\mathrm{M}_{\odot}$ for the hot subdwarf [Rigoselli et al., 2023]. The orbital velocity of the compact object was calculated from equation:

$$v_{\mathrm{X}} = \frac{2\pi a_{\mathrm{X}}}{P_{\mathrm{orb}}}, \tag{4.3}$$

where $a_{\mathrm{X}} = 2\,891\,000\,000\,\mathrm{m}$ is the aproximation of the semi-major axis of the compact object, calculated from $a_{\mathrm{X}} sin(i) = 9.60(5)$ light-second, with $i = 84.5°$ [Rigoselli et al., 2023], and $P_{\mathrm{orb}} = 1.548\,\mathrm{d}$ is the orbital period [Rigoselli et al., 2023]. Using this, the subdwarf's orbital velocity is $v_{\mathrm{HD}} = (117 \pm 8)\,\mathrm{km\,s^{-1}}$.

The next step would be to calculate the velocity from the Doppler shift of the line in N V doublet with shorter wavelength. The table value of this N V line wavelength, taken from NIST ASD [3], is $\lambda_0 = 1238.804\,$Å. Table 4.4 shows wavelengths of the NV line in the used data and calculated velocity using Doppler equation:

$$v = c\frac{\lambda - \lambda_0}{\lambda_0}, \tag{4.4}$$

where c is the speed of light. Velocities $v_{\mathrm{B}}$ were calculated using parameter B of the Gaussian and velocities $v_{\mathrm{edge}}$ using the blue edge of the line. The wavelength of the blue edge was calculated as $B - 3C$. Uncertainties for the velocities were calculated with the code using relative uncertainty of the wavelength according to the propagation of uncertainties.

Velocity $v_{\mathrm{edge}}$ does not completely align with the radial velocity curve and is much higher between phases 0.25 and 0.5. This changes could indicate interactions with the other compoent in the binary.

Both the stellar wind and the radial velocity contribute to the shifting of the spectral line. In order to obtain the stellar wind velocity, the radial velocity must be subtracted from the velocity calculated from the Doppler shift.

Terminal velocities of stellar wind, from both $v_{\mathrm{edge}}$ and $v_{\mathrm{B}}$, were calculated as:

$$v_{\infty} = v_{\mathrm{D}} - v_{\mathrm{rad}} - v_{\mathrm{s}}, \tag{4.5}$$

[3] https://physics.nist.gov/PhysRefData/ASD/lines_form.html

| **Data** | $\lambda_{\mathbf{edge}}$ | $v_{\mathbf{edge}}$ | $\lambda_B$ | $v_B$ | Phase |
|---|---|---|---|---|---|
| | [Å] | [km s$^{-1}$] | [Å] | [km s$^{-1}$] | - |
| swp01336HS | 1231.3(2) | -1812.2(3) | 1234.99(5) | -923.06(4) | 0.142502 |
| swp01698HS | 1232.3(1) | -1572.2(2) | 1235.06(4) | -904.99(3) | 0.382683 |
| swp01699HS | 1232.2(1) | -1605.4(1) | 1234.98(4) | -924.73(3) | 0.428527 |
| swp02513HS | 1231.1(2) | -1870.2(3) | 1234.49(6) | -1042.81(5) | 0.684046 |
| swp04024HS | 1230.7(2) | -1964.3(4) | 1234.71(7) | -990.25(6) | 0.915497 |
| swp04767HS | 1230.9(2) | -1919.8(4) | 1234.62(8) | -1011.54(6) | 0.549404 |
| swp04768HS | 1231.0(2) | -1886.5(4) | 1234.67(8) | -1000.41(6) | 0.763643 |
| swp04773HS | 1230.7(3) | -1953.9(5) | 1234.81(9) | -967.57(7) | 0.866087 |
| swp04776HS | 1230.5(3) | -2008.4(4) | 1234.69(8) | -996.71(6) | 0.934100 |
| swp04779HS | 1231.0(2) | -1886.4(4) | 1234.62(7) | -1013.40(6) | 0.980763 |
| swp04798HS | 1231.3(4) | -1819.1(7) | 1235.37(14) | -830.76(10) | 0.180305 |
| swp04802HS | 1231.8(2) | -1690.1(3) | 1235.08(7) | -902.04(5) | 0.252614 |
| swp05478HS | 1232.0(3) | -1655.4(4) | 1235.05(10) | -909.53(7) | 0.229888 |
| swp05481HS | 1231.8(3) | -1705.9(4) | 1235.12(10) | -890.41(7) | 0.3120311 |

Table 4.4: Velocity from Doppler shift for the edge of the line and parameter B.

where $v_D$ is velocity determined from Doppler shift, either $v_B$ or $v_{edge}$, $v_{rad}$ is radial velocity corresponding to the phase and $v_s = 12.10\,\mathrm{km\,s^{-1}}$ is the system velocity [Pourbaix et al., 2004] [4]. Radial velocity was assumed to be a sine function with amplitude equal to the orbital velocity $v_{HD}$ and phase shift previously calculated. The results are shown in table 4.5 and figure 4.5.

In the figure 4.5, radial velocity was shifted to mean value of velocity calculated from Doppler shift. Velocities $v_{\infty B}$ and $v_{\infty edge}$ represent the terminal velocity of the stellar wind. The average values of terminal velocities $\overline{v_{\infty B}} = (-977 \pm 48)\,\mathrm{km\,s^{-1}}$ and $\overline{v_{\infty edge}} = (-1837 \pm 95)\,\mathrm{km\,s^{-1}}$. Velocity $\overline{v_{\infty edge}}$ seems to be phase dependant, possibly due to interactions with the companion star.

### 4.2.5 Calculation of X-ray flux

Using these values with equation 1.1 we get the flux $L_X$. All quantities used in the calculation and their values are in the table 4.6. Values for $M_X$ and $R_X$, assuming white dwarf, were taken from [Rigoselli et al., 2023, Mereghetti and La Palombara, 2016, Mereghetti et al., 2021].

For the values from from the blue edge of the line, $L_{X\,edge} = (9.5 \pm 0.1) \times 10^{30}\,\mathrm{erg\,s^{-1}}$ which is over by an order lower than the observed value $L_{X\,obs} = (1.3 \pm 0.3) \times 10^{32}\,\mathrm{erg\,s^{-1}}$ [Mereghetti and La Palombara, 2016]. For the values from parameter B, $L_{X\,B} = (1.19 \pm 0.03) \times 10^{32}\,\mathrm{erg\,s^{-1}}$ which is very close to the observed value and belongs to its interval of uncertainty.

Several factors might have influenced the calculation. Firstly, the nature of the companion and its radius is still unknown. Using another value, $R_X = 3340\,\mathrm{km}$ [Popov et al., 2018], lowers the flux determined from parameter B to $L_{X\,B} = (5.7 \pm 0.3) \times 10^{31}\,\mathrm{erg\,s^{-1}}$.

[4] Source: SIMBAD

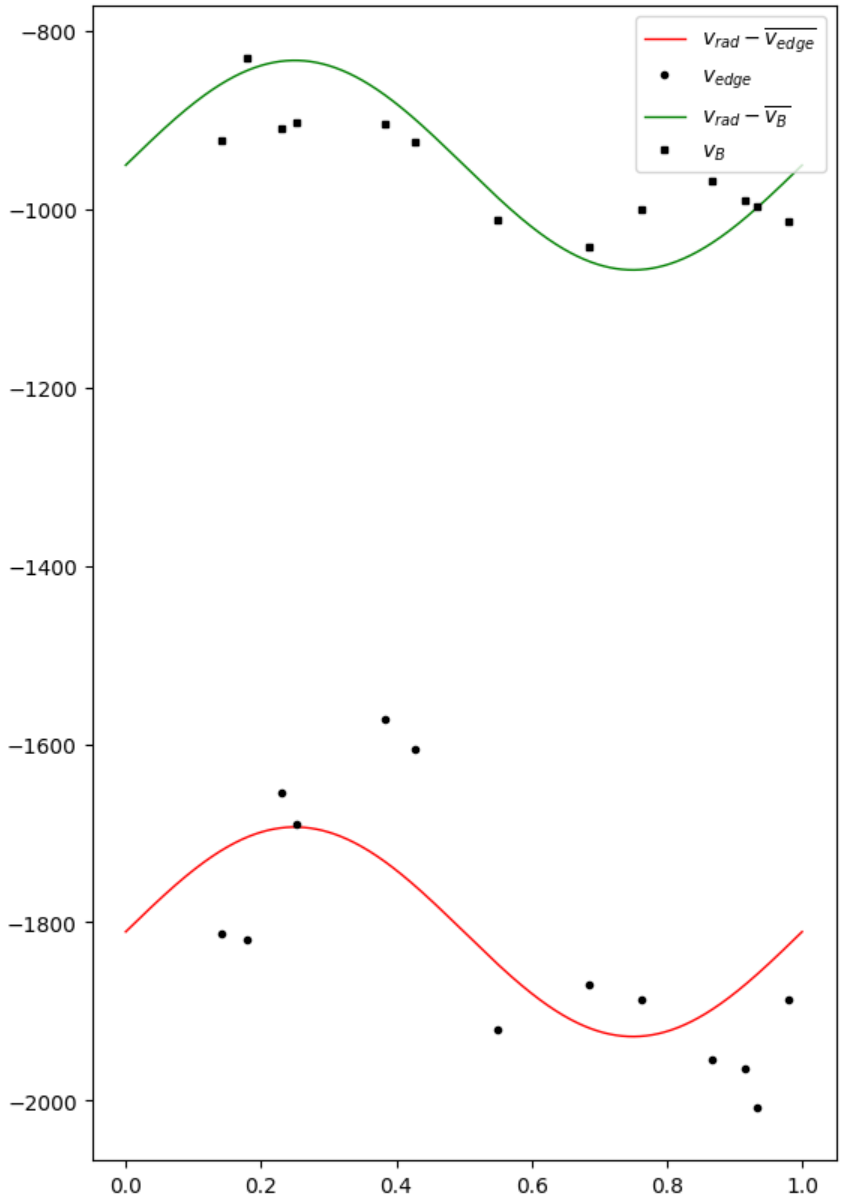


Figure 4.4: Velocities calculated from the Doppler shift over phase and radial velocity

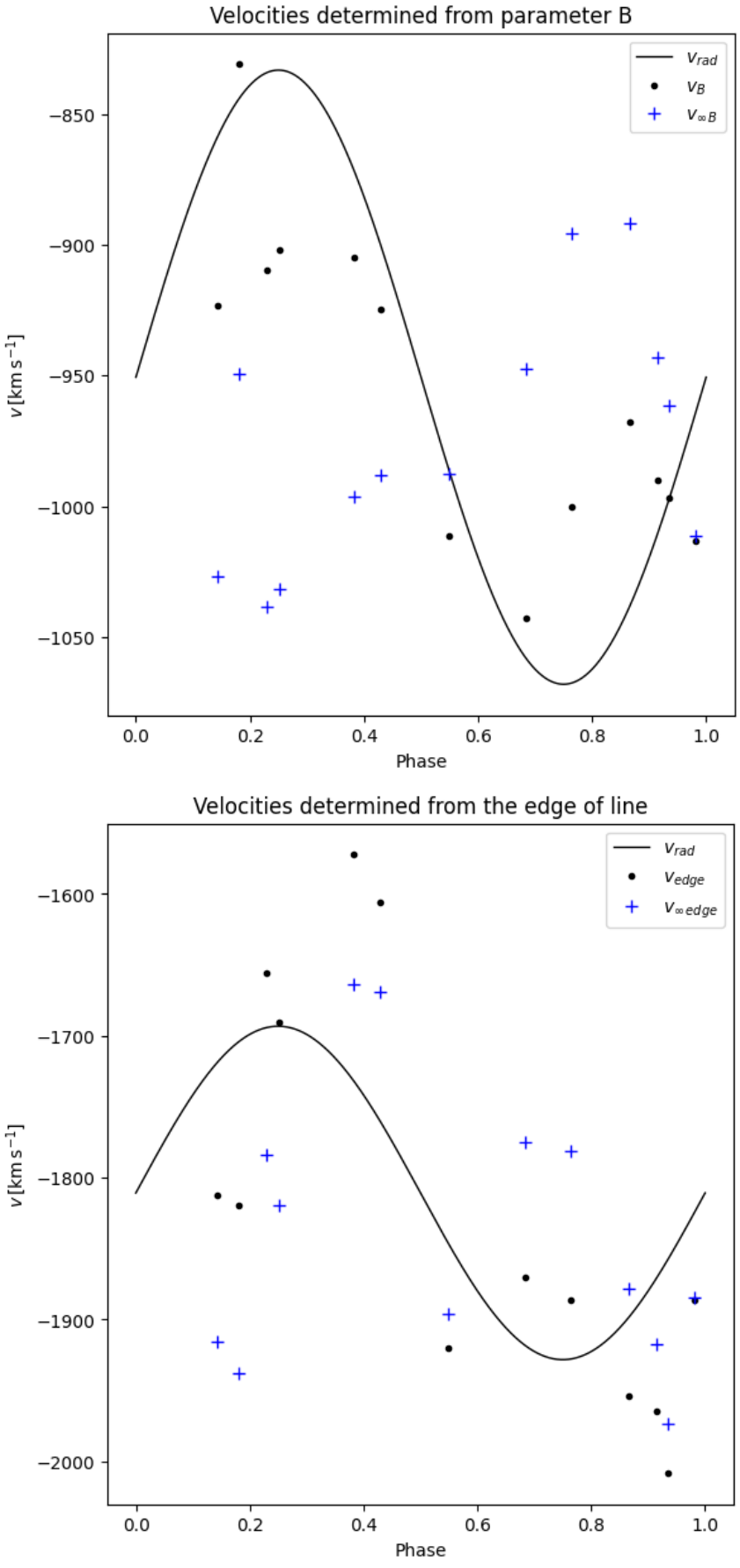


Figure 4.5: Velocities of the stellar wind

| Data | $v_{rad}$ | $v_{edge}$ | $v_{\infty edge}$ | $v_B$ | $v_{\infty B}$ | Phase |
|---|---|---|---|---|---|---|
| - | $km\,s^{-1}$ | $km\,s^{-1}$ | $km\,s^{-1}$ | $km\,s^{-1}$ | $km\,s^{-1}$ | - |
| swp01336HS | 92(6) | -1812.2(3) | -1916(6) | -923.06(4) | -1027(6) | 0.142502 |
| swp01698HS | 79(5) | -1572.2(2) | -1663(5) | -904.99(3) | -996(5) | 0.382683 |
| swp01699HS | 51(3) | -1605.4(1) | -1669(3) | -924.73(3) | -988(3) | 0.428527 |
| swp02513HS | -108(7) | -1870.2(3) | -1775(7) | -1042.81(5) | -947(7) | 0.684046 |
| swp04024HS | -59(4) | -1964.3(4) | -1917(4) | -990.25(6) | -943(4) | 0.915497 |
| swp04767HS | -36(2) | -1919.8(4) | -1896(3) | -1011.54(6) | -988(2) | 0.549404 |
| swp04768HS | -117(8) | -1886.5(4) | -1782(8) | -1000.41(6) | -895(8) | 0.763643 |
| swp04773HS | -87(6) | -1953.9(5) | -1878(6) | -967.57(7) | -892(6) | 0.866087 |
| swp04776HS | -47(3) | -2008.4(4) | -1973(3) | -996.71(6) | -961(3) | 0.934100 |
| swp04779HS | -14(1) | -1886.4(4) | -1885(1) | -1013.40(6) | -1012(1) | 0.980763 |
| swp04798HS | 106(7) | -1819.1(7) | -1938(7) | -830.76(10) | -949(7) | 0.180305 |
| swp04802HS | 117(8) | -1690.1(3) | -1820(8) | -902.04(5) | -1032(8) | 0.252614 |
| swp05478HS | 116(8) | -1655.4(4) | -1784(8) | -909.53(7) | -1038(8) | 0.229888 |
| swp05481HS | 109(7) | -1705.9(4) | -1827(7) | -890.41(7) | -1011(7) | 0.3120311 |

Table 4.5: Velocities of the stellar wind

| Quantity | Value |
|---|---|
| $M_X$ | $1.22\,M_\odot$ |
| $R_X$ | 1600 km |
| $v_{orb}$ | $117(8)\,km\,s^{-1}$ |
| $\overline{v_{\infty B}}$ | $-977(48)\,km\,s^{-1}$ |
| $\overline{v_{\infty edge}}$ | $-1837(95)\,km\,s^{-1}$ |

Table 4.6: Values used for calculation of X-ray luminosity

Furthermore, more unknown processes might influence the stellar wind and the accretion, such as previously mentioned X-ray photoionisation suggested by [Krtička et al., 2019]. Another thing that can strongly influence the final results is that the spectra don't seem to be saturated, which complicates the process. Saturated P Cygni spectra should have sharp difference between the line and the continuum and zero intensity only at $v_\infty$ [Prinja et al., 1990] which is not the case with the spectra used. Due to this, it is questionable to which wavelength to use to calculate the terminal velocity, therefore both parameter B and blue edges of N V lines were used. Moreover, $Ly\,\alpha$ lines in the spectra suggest that, in case they are saturated, they might have been incorrectly processed. In such case, parameter B is a better choice for determining the terminal velocity and $L_X$.

Incorrect estimates and parameters could be another source of difference.

# Conclusion

In this thesis we analyzed ultraviolet spectra od HD 49798 from space observatory IUE. We identified the most prominent spectral lines, among them the short-wavelength component of N V doublet on which we further focused. The blue edge of this line was fitted using Gaussian and obtained parameters were used to plot the phase diagrams. Out of them, parameter B representing the shift wavelength showed phase dependence, which is most likely due to its relation to the orbital velocity.

In the following section, semiamplitude of orbital velocity was calculated using stellar parameters from [Rigoselli et al., 2023] and we obtained result $v_{\mathrm{orb}} = (117 \pm 8)\,\mathrm{km\,s^{-1}}$. Other than $v_{\mathrm{rad}}$, velocity from Doppler shift was needed to get to the terminal velocity $v_{\infty}$. We obtained Doppler shift velocities from wavelength of parameter B and the blue edge of the line. After subtracting radial velocities from Doppler shift velocities, we were finally able to obtain wind velocities. They weren't constant as expected, but rather scattered around with a large standard deviation. Therefore a mean value was calculated and considered as the final terminal velocity.

Using both velocities $\overline{v_{\infty\mathrm{B}}} = (-977 \pm 48)\,\mathrm{km\,s^{-1}}$ and $\overline{v_{\infty\mathrm{edge}}} = (-1837 \pm 95)\,\mathrm{km\,s^{-1}}$, and assuming the compact companion is white dwarf, we were able to calculate the X-ray luminosity $L_{\mathrm{X}}$. Luminosity $L_{\mathrm{X\ edge}} = (9.5 \pm 0.1) \times 10^{30}\,\mathrm{erg\,s^{-1}}$ is lower than the observed value $L_{\mathrm{X\ obs}} = (1.3 \pm 0.3) \times 10^{32}\,\mathrm{erg\,s^{-1}}$ [Mereghetti and La Palombara, 2016]. However the luminosity calculated using parameter B gives value belonging to the observed $L_{\mathrm{X}}$'s interval of uncertainty - $L_{\mathrm{X\,B}} = (1.19 \pm 0.03) \times 10^{32}\,\mathrm{erg\,s^{-1}}$. Therefore calculated terminal velocity is consistent with the observations.

Several factors might have influenced the results and they are debated in the discussion of the last chapter. Thus, we managed to resolve the issue of the X-ray emission strength from HD 49798 through a precise measurement of its wind terminal velocity.

Further research and new measurements are highly recommended as it would help us understand better not only HD 49798 itself, but also similar binaries with stellar wind and possibly even young contracting white dwarfs.

# Appendix

## 4.3 Code

```
#IMPORT PACKAGES

import numpy as np
import pandas as pd
import matplotlib.pyplot as plt
from astropy.io import fits
import scipy
from scipy.optimize import curve_fit
from scipy import asarray as ar,exp
import statistics as stat


#DATA

data_1="Data/swp01336HS.fits"
hdul_1=fits.open(data_1)
header_1 = hdul_1[0].header
#datum merania: 1978-04-08 09:35:00
Time_1 = 43607.41328 #modified Julian date of mid exposure

data_2="Data/swp01698HS.fits"
hdul_2=fits.open(data_2)
header_2 = hdul_2[0].header
#datum merania: 1978-06-01 22:42:33
Time_2 = 43661.95331

data_3="Data/swp01699HS.fits"
hdul_3=fits.open(data_3)
header_3 = hdul_3[0].header
#datum merania: 1978-06-02 00:20:00
Time_3 = 43662.02426


data_4="Data/swp02513HS.fits"
hdul_4=fits.open(data_4)
```

```
header_4 = hdul_4[0].header
#datum merania: 1978-09-06 08:53:00
Time_4 = 43758.37501

data_5="Data/swp04024HS.fits"
hdul_5=fits.open(data_5)
header_5 = hdul_5[0].header
#datum merania: 1979-01-24 00:21:13
Time_5 = 43898.02316

data_6="Data/swp04767HS.fits"
hdul_6=fits.open(data_6)
header_6 = hdul_6[0].header
#datum merania: 1979-03-26 15:43:13
Time_6 = 43595.6617

data_7="Data/swp04768HS.fits"
hdul_7=fits.open(data_7)
header_7 = hdul_7[0].header
#datum merania: 1979:03-26 16:31:08
Time_7 = 43959.69478

data_8="Data/swp04773HS.fits"
hdul_8=fits.open(data_8)
header_8 = hdul_8[0].header
#datum merania: 1979-03-26 20:19:27
Time_8 = 43959.85333

data_9="Data/swp04776HS.fits"
hdul_9=fits.open(data_9)
header_9 = hdul_9[0].header
#datum merania: 1979-03-26 22:52:02
Time_9 = 43959.95859

data_10="Data/swp04779HS.fits"
hdul_10=fits.open(data_10)
header_10 = hdul_10[0].header
#datum merania: 1979-03-27 00:26:02
Time_10 = 43960.03081

data_11="Data/swp04798HS.fits"
hdul_11=fits.open(data_11)
header_11 = hdul_11[0].header
Time_11 = 43961.88730

data_12="Data/swp04802HS.fits"
hdul_12=fits.open(data_12)
header_12 = hdul_12[0].header
```

```
#datum merania: 1979-03-28 23:49:38
Time_12 = 43961.99921

data_13="Data/swp05478HS.fits"
hdul_13=fits.open(data_13)
header_13 = hdul_13[0].header
#datum merania: 1979-06-09 16:49:34
Time_13 = 44034.70434

data_14="Data/swp05481HS.fits"
hdul_14=fits.open(data_14)
header_14 = hdul_14[0].header
#datum merania: 1979-06-09 19:52:38
Time_14 = 44034.83147


data_all=[data_1,data_2,data_3,data_4,data_5,data_6,data_7,data_8,
    data_9,data_10,data_11,data_12,data_13,data_14]

hdul_all=[hdul_1,hdul_2,hdul_3,hdul_4,hdul_5,hdul_6,hdul_7,hdul_8,hdul_9,
    hdul_10,hdul_11,hdul_12,hdul_13,hdul_14]

header_all=[header_1,header_2,header_3,header_4,header_5,header_6,
header_7,header_8,header_9,header_10,header_11,header_12,header_13,
    header_14]

Time_all=[Time_1,Time_2,Time_3,Time_4,Time_5,Time_6,Time_7,Time_8,Time_9,
    Time_10,Time_11,Time_12,Time_13,Time_14]


#FLUX AND WAVELENGTH FILES
#The first one is "flux_0" and the last one is "flux_13


flux_all = {}
wave_all = {}
i = 0
for i in range(len(hdul_all)):
    flux_all[f'flux_{i}'] = hdul_all[i][0].data
    globals()[f'flux_{i}'] = hdul_all[i][0].data


    wavelength = []
    j = 1 # Start at L1_A
    while f"L{j}_A" in header_all[i]:
        wavelength.append(header_all[i][f"L{j}_A"])
        j += 1
```

```
    wave_all[f'wave_{i}'] = wavelength
    globals()[f'wave_{i}'] = wavelength


#FIT DEFINTION

def fit(xdata, ydata, wavelength, flux, name):


    def gauss (x,y0,B,C,A): #Definition of the function
        y=y0-A*exp(-(x-B)**2/(2*C)**2)
        return (y)

    #Initial guess of parameters
    initial_y0 = np.mean(ydata)
    initial_B = xdata[np.argmin(ydata)]
    initial_C = (np.max(xdata) - np.min(xdata)) / 4
    initial_A = np.max(ydata) - initial_y0

    parameters, covariance =
        curve_fit(gauss, xdata, ydata, p0=[initial_y0, initial_B,
        initial_C, initial_A], maxfev=2000)

    fit_y0 = parameters[0] #continuum
    fit_B = parameters[1] #wavelength of the line center
    fit_C = parameters[2] #standard deviation
    fit_A = parameters[3] #amplitude (flux)

    uncertainty = np.sqrt(np.diag(covariance))
    uncertainty_y0 = uncertainty[0]
    uncertainty_B = uncertainty[1]
    uncertainty_C = uncertainty[2]
    uncertainty_A = uncertainty[3]

    fit_y = gauss(xdata, fit_y0, fit_B, fit_C, fit_A)
    G = gauss(wavelength, fit_y0, fit_B, fit_C, fit_A)

    #print('y_0 = ', fit_y0, "+-", uncertainty_y0)

    min_flux.append(np.min(fit_y))


    y0_all.append(fit_y0)
    A_all.append(fit_A)
    B_all.append(fit_B)
    C_all.append(fit_C)
    width_all.append(np.abs(fit_C)*6)
```

```
    #UNCERTAINTIES
    uncertainty_A_all.append(uncertainty_A)
    uncertainty_B_all.append(uncertainty_B)
    uncertainty_C_all.append(uncertainty_C)
    uncertainty_y0_all.append(uncertainty_y0)
    uncertanrtinty_width_all.append(uncertainty_C*6)



#PLOT
    plt.ylim(0, 2E-10)
    plt.plot(wavelength[2000:4000], flux[2000:4000], linewidth=1)
    plt.plot(xdata, ydata, '-')
    plt.plot(wavelength[2000:4000],G[2000:4000],'-',color='yellow')
    plt.plot(xdata, fit_y, '-', color='magenta')
    plt.legend(["Flux", "Line", "Gaussian", "Fit"])
    plt.title(name)
    plt.xlabel('wavelength␣[]')
    plt.ylabel('flux␣[$\mathrm{erg␣\,␣s^{-1}␣\,␣cm^{-2}␣\,␣^{-1}}$]')
    plt.show()


#ACTUAL FITTING

#this has to stay here and be empty before the loop
y0_all = []
A_all = []
B_all = []
C_all = []
width_all = []


uncertainty_A_all = []
uncertainty_B_all = []
uncertainty_C_all = []
uncertainty_y0_all = []
uncertanrtinty_width_all = []


min_flux=[]
min_wave=[]
#the lists have to be empty before the loop


fit(wave_0[2620:2800], flux_0[2620:2800], wave_0, flux_0, 'swp01336HS')
fit(wave_1[2620:2800], flux_1[2620:2800], wave_1, flux_1, 'swp01698HS')
fit(wave_2[2620:2800], flux_2[2620:2800], wave_2, flux_2, 'swp01699HS')
```

```
fit(wave_3[2550:2800], flux_3[2550:2800], wave_3, flux_3, 'swp02513HS')
fit(wave_4[2570:2800], flux_4[2570:2800], wave_4, flux_4, 'swp04024HS')
fit(wave_5[2570:2800], flux_5[2570:2800], wave_5, flux_5, 'swp04767HS')
fit(wave_6[2570:2800], flux_6[2570:2800], wave_6, flux_6, 'swp04768HS')
fit(wave_7[2570:2800], flux_7[2570:2800], wave_7, flux_7, 'swp04773HS')
fit(wave_8[2570:2800], flux_8[2570:2800], wave_8, flux_8, 'swp04776HS')
fit(wave_9[2570:2800], flux_9[2570:2800], wave_9, flux_9, 'swp04779HS')
fit(wave_10[2620:2800], flux_10[2620:2800], wave_10, flux_10,'swp04798HS')
fit(wave_11[2620:2800], flux_11[2620:2800], wave_11, flux_11,'swp04802HS')
fit(wave_12[2550:2800], flux_12[2550:2800], wave_12, flux_12,'swp05478HS')
fit(wave_13[2620:2800], flux_13[2620:2800], wave_13, flux_13,'swp05481HS')


#THIS HAS TO STAY HERE
C_abs_all=np.abs(C_all)


#TABLE WITH FIT RESULTS

table = pd.DataFrame()
table['y0'] = y0_all
table['uncertainty_y0'] = uncertainty_y0_all
table['A'] = A_all
table['uncertainty_A'] = uncertainty_A_all
table['B'] = B_all
table['uncertainty_B'] = uncertainty_B_all
table['C'] = C_all
table['uncertainty_C'] = uncertainty_C_all

table['y0']=table['y0']*1E11
table['A']=table['A']*1E11

print(table)
print('y0 = ',np.mean(y0_all),
'+-',np.sqrt((np.mean(table['uncertainty_y0']))**2
+ (stat.stdev(table['uncertainty_y0']))**2))

print('A = ',np.mean(A_all),
'+-',np.sqrt((np.mean(table['uncertainty_A']))**2
+ (stat.stdev(table['uncertainty_A']))**2))

print('B = ',np.mean(B_all),
'+-',np.sqrt((np.mean(table['uncertainty_B']))**2
+ (stat.stdev(table['uncertainty_B']))**2))

print('C = ',np.mean(C_all),
'+-',np.sqrt((np.mean(table['uncertainty_C']))**2
+ (stat.stdev(table['uncertainty_C']))**2))
```

```
#AVERAGE VALUES OF THE PARAMETERS
print('Average␣values:␣y0␣=␣', np.average(y0_all),'....␣A␣=␣',
np.average(A_all),
'.....␣B␣=␣', np.average(B_all),
'.......␣C␣=␣', np.average(C_all))


#PLOT PARAMETERS OVER TIME (MODIFIED JULIAN DATE OF MID EXPOSURE)


plt.figure().set_figheight(20)
plt.figure().set_figwidth(10)
plt.errorbar(Time_all,y0_all, yerr=uncertainty_y0_all, fmt='.k')
plt.xlabel('Time␣[MJD]')
plt.ylabel('$y_0$␣[$\mathrm{erg␣\,␣s^{-1}␣\,␣cm^{-2}␣\,␣^{-1}}$]')
plt.title('Value␣of␣continuum', fontsize=14)
#plt.text(0.5,0.5,'Parameter y_0')
plt.show()

plt.figure().set_figheight(20)
plt.figure().set_figwidth(10)
plt.errorbar(Time_all,A_all, yerr=uncertainty_A_all, fmt='.k')
plt.title('Amplitude', fontsize=14)
#plt.text(0.5,0.5,'Parameter y_0')
plt.xlabel('Time␣[MJD]')
plt.ylabel('A␣␣[$\mathrm{erg␣\,␣s^{-1}␣\,␣cm^{-2}␣\,␣^{-1}}$]')
plt.show()

plt.figure().set_figheight(20)
plt.figure().set_figwidth(10)
plt.errorbar(Time_all,B_all, yerr=uncertainty_B_all, fmt='.k')
plt.title('Wavelength␣shift')
#plt.text(0.5,0.5,'Parameter B')
plt.xlabel('Time␣[MJD]')
plt.ylabel('B␣[]')
plt.show()

plt.figure().set_figheight(20)
plt.figure().set_figwidth(10)
plt.errorbar(Time_all,C_abs_all, yerr=uncertainty_C_all, fmt='.k')
plt.title('Standard␣deviation␣of␣the␣Gaussian', fontsize=14)
#plt.text(0.5,0.5,'Parameter C')
plt.xlabel('Time␣[MJD]')
plt.ylabel('C␣[]')
plt.show()
```

```
#TIME TO PHASE CONVERSION
P_orb=1.547666 #[d] ... Rigoselli 2023 133718.3424 #[s]
unc_P_orb=0.000006

# MJD 59 186.406(1) --> phase 0.75
t_0 = 54597.169 #time in MJD with phase = '0' = 1

phase_new=[]
i=0
for i in range(len(Time_all)):
    phase_new.append(((Time_all[i]-t_0)/P_orb)-((Time_all[i]-t_0))//P_orb)
    #print(round(phase_new[i],7))
    i=i+1


#PARAMETERS OVER PHASE


ph_hd_all=[]



for i in range(len(Time_all)):
    ph_hd_all.append(((Time_all[i]
    -Time_all[0])/P_orb)-((Time_all[i]-Time_all[0])//P_orb))
    i=i+1


def phase_plot(x,y, yerr, name, parameter):

    plt.figure().set_figheight(20)
    plt.figure().set_figwidth(10)
    plt.errorbar(x,y, yerr=yerr, fmt='.k')
    plt.xlabel('Phase')
    plt.ylabel(parameter)
    plt.title(name)
    plt.show()



#ORBITAL PERIOD OF SUBDWARF
phase_plot(phase_new[0:13], y0_all[0:13], uncertainty_y0_all[0:13],
'Value␣of␣continuum' ,'y0␣[$\mathrm{erg␣\,␣s^{-1}␣\,␣cm^{-2}␣\,␣^{-1}}$]')

phase_plot(phase_new[0:13], A_all[0:13], uncertainty_A_all[0:13],
'Amplitude' ,'A␣[$\mathrm{erg␣\,␣s^{-1}␣\,␣cm^{-2}␣\,␣^{-1}}$]')
```

```
phase_plot(phase_new[0:13], B_all[0:13], uncertainty_B_all[0:13],
'Wavelength␣of␣shift', 'B␣[]')

phase_plot(phase_new[0:13], C_abs_all[0:13], uncertainty_C_all[0:13],
'Standard␣deviation␣of␣Gaussian' ,'C␣[]')




#CALCULATION OF THE ORBITAL VELOCITY
P_orb_s = P_orb*(3600*24)
P_orb_yr=P_orb/365.25
                        #it was defined above


G=6.6743E-11 #m3 kg-1 s-2

M_X=1.220*(2E30) #+- 0.08*(2E30) [kg] Rigoselli 2023
unc_M_X=0.08*(2E30)

M_HD=1.41*(2E30) #+- 0.02*(2E30) [kg] Rigoselli 2023
unc_M_HD=0.02*(2E30)


a_X=2891000000 # 15000000 [m] Rigoselli 2023
unc_a_X=15000000

a=(((P_orb_yr**2)*(1.5+1.2))**(1/3))*(1.5E11) #a=a_x + a_HD
a_HD=a-a_X

v_HD=(M_X/M_HD)*(2*np.pi*a_X/P_orb_s) #orbit velocity of the subdwarf

unc_v_HD=np.sqrt((unc_M_X/M_X)**2+(unc_M_HD/M_HD)**2
+(unc_a_X/a_X)**2+(unc_P_orb/P_orb)**2)*v_HD



#RADIAL VELOCITY

x_axis = np.linspace(0, 1, 1000)
rad_v=v_HD/1000*(np.sin(2*np.pi*x_axis)) #km/s
unc_rad_v=np.abs((unc_v_HD/v_HD)*rad_v)

c=299792458

w_0=1238.804 #tabular value of NV line in  (source: NIST ASD)

i=0
```

```
def doppler (w):
    v_all

    for i in range(len(w)):


        v=c*((w[i]-w_0)/w_0)
        v_all.append(v)

#DETERMIMING THE EDGE OF THE LINE
beg_all=[]
i=0

for i in range(len(B_all)):
    beg_all.append(B_all[i]
    -np.abs((3*C_all[i])))
    #middle of the line - 3*standard deviation

    i=i+1


#UNCERTAINTY OF THE EDGE OF THE LINE
unc_beg_all=[]
for i in range(len(beg_all)):
    unc_beg_all.append(np.sqrt((uncertainty_B_all[i])**2
    +3*(uncertainty_C_all[i])**2))
    #+- 3*uncertainty of the standard deviation

    i=i+1

#VELOCITY FROM THE DOPPLER SHIFT OF THE EDGE OF THE LINE
v_all=[]
doppler(beg_all)
v_beg_all=np.array(v_all)
v_beg_all=v_beg_all/1000 #m/s to km/s

unc_v_beg_all=[]
i=0
for i in range(len(v_beg_all)):
    unc_v_beg_all.append(np.abs(unc_beg_all[i]/beg_all[i]*v_beg_all[i]))
    #uncertainty of the velocity from the edge of the line

    i=i+1


#relative uncertainty 0.0002
```

```
#VELOCITY FROM THE DOPPLER SHIFT OF THE CENTER OF THE LINE
v_all=[]
doppler(B_all)
v_B_all=np.array(v_all)
v_B_all=v_B_all/1000 #m/s to km/s

unc_v_B_all=[]
i=0
for i in range(len(v_B_all)):
    unc_v_B_all.append(np.abs(uncertainty_B_all[i]/B_all[i]*v_B_all[i]))
    #uncertainty of the velocity from the center of the line

    i=i+1

#TABLE WITH VELOCITY AND WAVELENGTH VALUES

table_2 = pd.DataFrame()
table_2['\lambda_{edge}'] = beg_all
table_2['uncertainty_{edge}'] = unc_beg_all
table_2['v_{edge}']= v_beg_all
table_2['uncertainty_{v\,edge}'] = unc_v_beg_all
table_2['\lambda_{B}'] = B_all
table_2['uncertainty_{B}'] = uncertainty_B_all
table_2['v_{B}']= v_B_all
table_2['uncertainty_{v\,␣B}'] = unc_v_B_all

print(table_2)



rad_v_list=[]
unc_rad_v_list=[]

#just assigning radial velocities to the phases because i need a list with
only a few points
for i in range(14):
    for j in range (len(x_axis)):
        if (x_axis[j] in pd.Interval(left=phase_new[i]
        -0.0005, right=phase_new[i]+0.0005))==True:
            #print ('YES', i, j)
            rad_v_list.append(rad_v[j])
            unc_rad_v_list.append(unc_rad_v[j])

            j=0

        else:
            j=j+1
    i=i+1
```

```
#calculated velocity = radial velocity - wind velocity;
however we assume wind velocity is negative because it moves towards us
so it turns to calculated = radial + wind


velocities_B=v_B_all-rad_v_list
velocities_beg=v_beg_all-rad_v_list

unc_vel_B=[]
unc_vel_beg=[]
i=0
for i in range(len(velocities_B)):
    unc_vel_B.append(np.sqrt((unc_v_B_all[i])**2+(unc_rad_v_list[i])**2))
    unc_vel_beg.append(np.sqrt((unc_v_beg_all[i])
    **2+(unc_rad_v_list[i])**2))
    i=i+1

print(np.mean(velocities_B),'+-',
np.sqrt((np.mean(unc_vel_B))**2+(stat.stdev(velocities_B))**2))

print(np.mean(velocities_beg),'+-',np.sqrt((np.mean(unc_vel_beg))**2
+(stat.stdev(velocities_beg))**2))


#PLOTS
points_x=[]
points_y=[]

#FROM CENTER OF THE LINE
plt.figure().set_figheight(7)
plt.plot(x_axis, rad_v+np.mean(v_B_all),linewidth=1, color='black')
#RADIAL VELOCITY IN KM/S SHIFTED BY AVERAGE WIND VELOCITY (just so graph
    looks pretty)
plt.plot(phase_new[0:13], v_B_all[0:13], 'o', markersize=3, color='black')
#plt.plot(phase_new[0:13], rad_v_list[0:13], 'o', markersize=3,
    color='red')
plt.plot(phase_new[0:13],velocities_B[0:13], '+', markersize=7,
    color='blue')
plt.xlabel('Phase')
plt.ylabel('$v\,\mathrm{[km\,s^{-1}}]$')
plt.legend(['$v_{rad}$','$v_B$', '$v_{\infty\,B}$'],loc="upper␣right")
plt.title('Velocities␣determined␣from␣parameter␣B')

#FROM THE EDGE OF THE LINE
plt.figure().set_figheight(7)
plt.plot(x_axis,rad_v+np.mean(v_beg_all),linewidth=1, color='black')
#RADIAL VELOCITY IN KM/S SHIFTED BY AVERAGE WIND VELOCITY
```

```
plt.plot(phase_new[0:13], v_beg_all[0:13], 'o', markersize=3,
    color='black')
#plt.plot(phase_new[0:13], rad_v_list[0:13], 'o', markersize=3,
    color='red')
plt.plot(phase_new[0:13],velocities_beg[0:13], '+', markersize=7,
    color='blue')
plt.xlabel('Phase')
plt.ylabel('$v\,\mathrm{[km\,s^{-1}}]$')
plt.legend(['$v_{rad}$','$v_{edge}$', '$v_{\infty\,edge}$'],loc="upper␣
    right")
plt.title('Velocities␣determined␣from␣the␣edge␣of␣line')

table_3 = pd.DataFrame()
table_3['$v_{rad}$']=rad_v_list
table_3['$v_{edge}$']=v_beg_all
table_3['$$v_\infty\,edge$']=velocities_beg
table_3['$v_B$']=v_B_all
table_3['$v_\infty\,B$']=velocities_B
table_3['phase']=phase_new


print(table_3)


G=6.6743E-11 #m3 kg-1 s-2
M_X=1.22*(1.989E30)
#mass of the companion in kg
mass_loss=2.1E-9*(1.989E30)/(3600*24*365.25)
#mass loss rate of the subdwarf in kg/s
a=5.7E9 #ax+aHD in m

def x_ray_flux(v, R_X):

    flux_x=(G*M_X/R_X)*(mass_loss)*((G*M_X)/(a*v**2))**2
    print('flux_x',flux_x, 'Watt')
    return flux_x


flux_x_edge=x_ray_flux(np.mean(velocities_beg)*1E3, 1600E3)
unc_x_flux=4*(np.mean(unc_vel_beg)/np.mean(velocities_beg))*flux_x_edge
#uncertainty of the flux from the edge of the line
print(unc_x_flux, 'Watt')

flux_x_B=x_ray_flux(np.mean(velocities_B)*1E3, 1600E3)
unc_x_flux_B=4*(np.mean(unc_vel_B)/np.mean(velocities_B))*flux_x_B
print('B', unc_x_flux_B, 'Watt')
```

Listing 4.1: Code used for data analysis

## 4.4 Fits

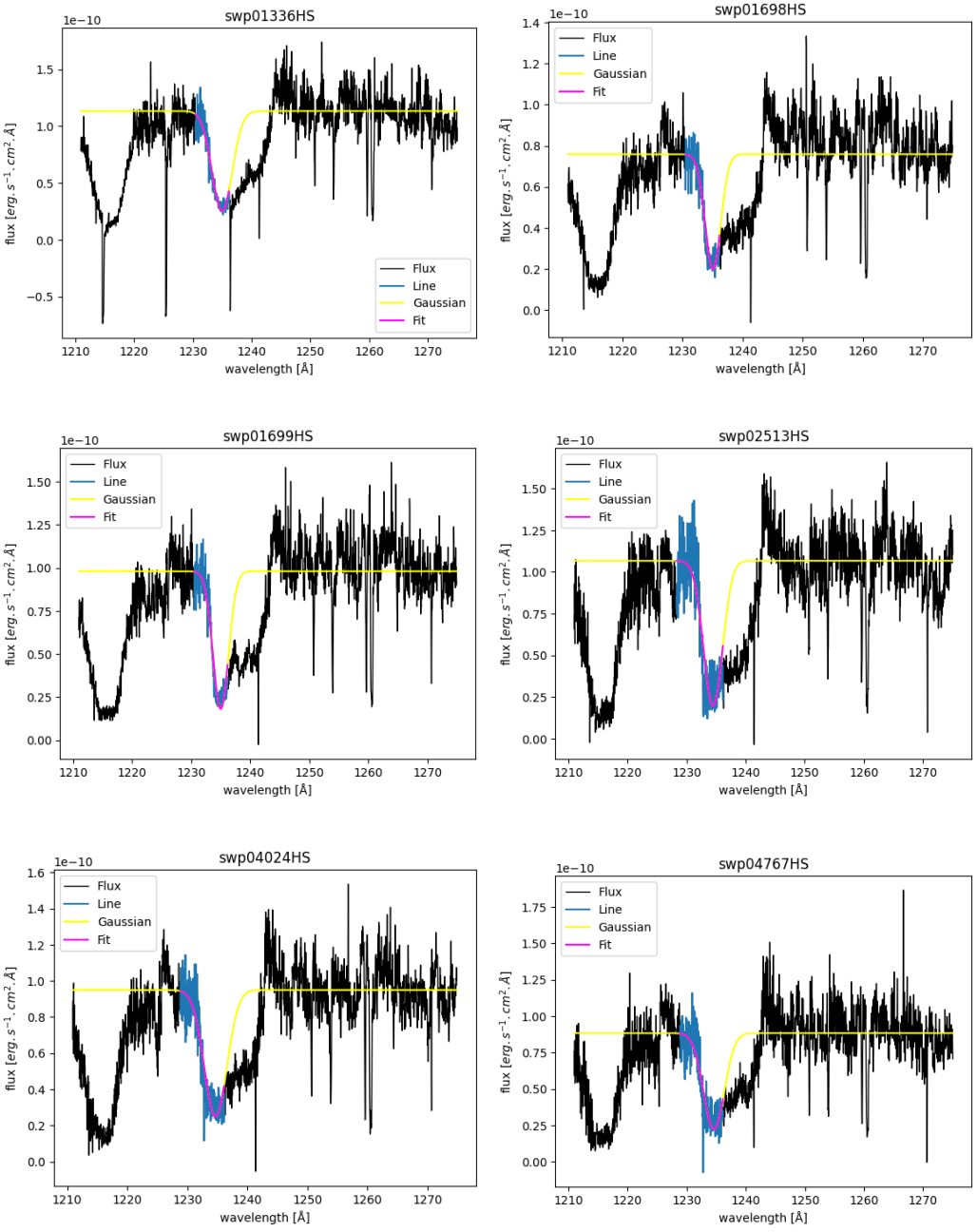
swp01336HS
swp01698HS
swp01699HS
swp02513HS
swp04024HS
swp04767HS
1e−10
flux [erg.s⁻¹.cm².Å]
wavelength [Å]
Flux
Line
Gaussian
Fit

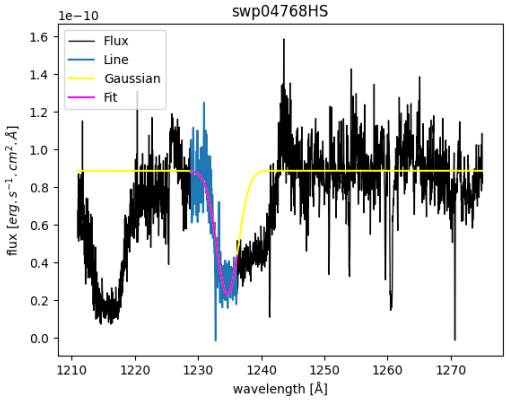
swp04768HS
1e−10
Flux
Line
Gaussian
Fit
flux [erg.s⁻¹.cm².Å]
wavelength [Å]

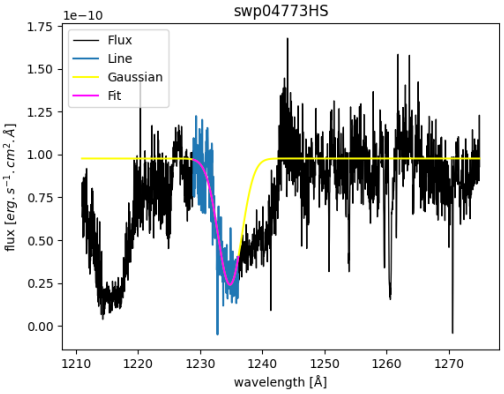
swp04773HS
1e−10
Flux
Line
Gaussian
Fit
flux [erg.s⁻¹.cm².Å]
wavelength [Å]

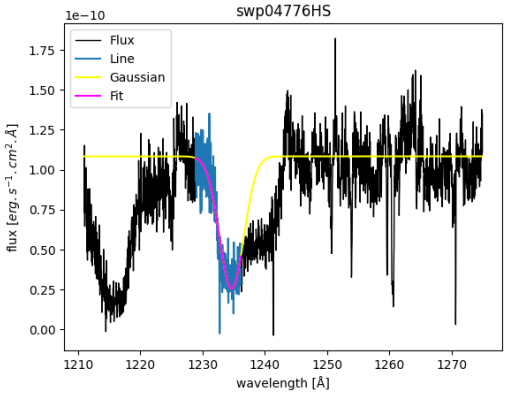
swp04776HS
1e−10
Flux
Line
Gaussian
Fit
flux [erg.s⁻¹.cm².Å]
wavelength [Å]

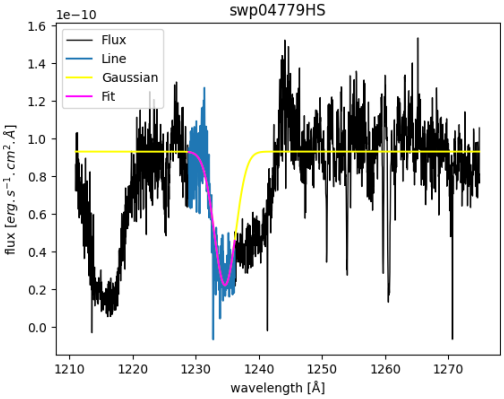
swp04779HS
1e−10
Flux
Line
Gaussian
Fit
flux [erg.s⁻¹.cm².Å]
wavelength [Å]

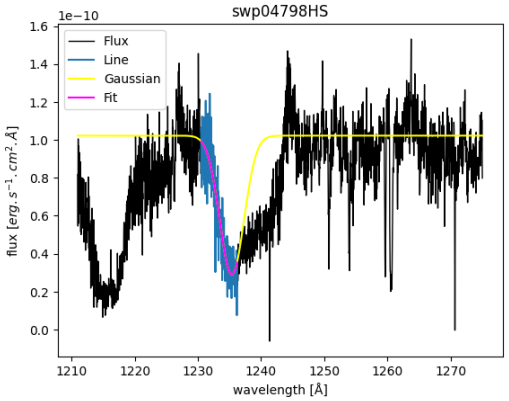
swp04798HS
1e−10
Flux
Line
Gaussian
Fit
flux [erg.s⁻¹.cm².Å]
wavelength [Å]

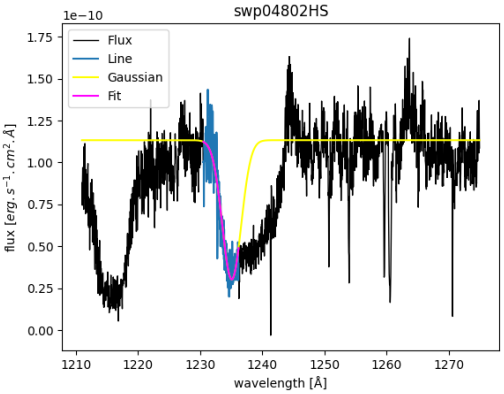
swp04802HS
1e−10
Flux
Line
Gaussian
Fit
flux [erg.s⁻¹.cm².Å]
wavelength [Å]

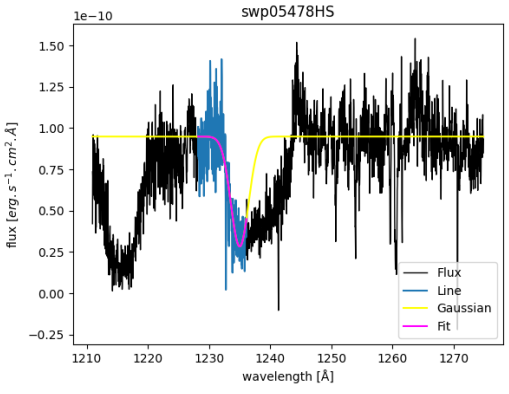
swp05478HS
1e−10
Flux
Line
Gaussian
Fit
flux [erg.s⁻¹.cm².Å]
wavelength [Å]

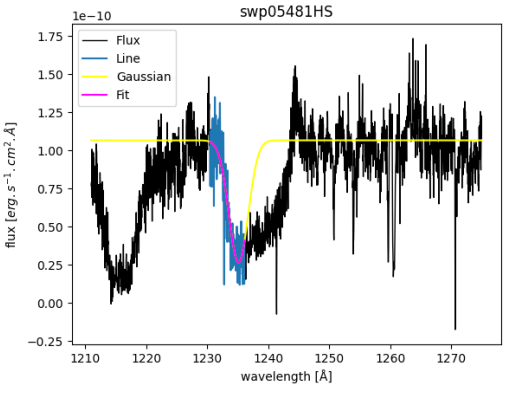
swp05481HS
1e−10
Flux
Line
Gaussian
Fit
flux [erg.s⁻¹.cm².Å]
wavelength [Å]

# Bibliography


D. C. Abbott and L. B. Lucy. Multiline transfer and the dynamics of stellar winds. , 288:679–693, January 1985. doi: 10.1086/162834.

I. I. Antokhin, G. Rauw, J. M. Vreux, K. A. van der Hucht, and J. C. Brown. XMM-Newton X-ray study of early type stars in the Carina OB1 association. , 477(2):593–609, January 2008. doi: 10.1051/0004-6361:20065711.

Martin Asplund, Nicolas Grevesse, A. Jacques Sauval, and Pat Scott. The Chemical Composition of the Sun. , 47(1):481–522, September 2009. doi: 10.1146/annurev.astro.46.060407.145222.

Jared Brooks, Thomas Kupfer, and Lars Bildsten. HD 49798: Its History of Binary Interaction and Future Evolution. , 847(1):78, September 2017. doi: 10.3847/1538-4357/aa87b3.

Santi Cassisi, Helmut Schlattl, Maurizio Salaris, and Achim Weiss. First Full Evolutionary Computation of the Helium Flash-induced Mixing in Population II Stars. , 582(1):L43–L46, January 2003. doi: 10.1086/346200.

M. Castellani and V. Castellani. Mass Loss in Globular Cluster Red Giants: an Evolutionary Investigation. , 407:649, April 1993. doi: 10.1086/172547.

J. I. Castor, D. C. Abbott, and R. I. Klein. Radiation-driven winds in Of stars. , 195:157–174, January 1975. doi: 10.1086/153315.

Drew Clausen and Richard A. Wade. How to Make a Singleton sdB Star via Accelerated Stellar Evolution. , 733(2):L42, June 2011. doi: 10.1088/2041-8205/733/2/L42.

H. T. Şener and C. S. Jeffery. Spectroscopic orbital elements for the helium-rich subdwarf binary PG 1544+488. , 440(3):2676–2683, May 2014. doi: 10.1093/mnras/stu397.

J. E. Drew. Ionization and Thermal Equilibrium Models for O Star Winds Based on Time-independent Radiation-driven Wind Theory. , 71:267, October 1989. doi: 10.1086/191374.

H. Edelmann, U. Heber, R. Napiwotzki, I. N. Reid, and R. A. Saffer. Spectral analysis of the binary sdB star Feige 36. In S. E. Solheim and E. G. Meistas, editors, *11th European Workshop on White Dwarfs*, volume 169 of *Astronomical Society of the Pacific Conference Series*, page 546, January 1999.

H. Edelmann, U. Heber, and R. Napiwotzki. Metal abundances of sdB stars. *Astronomische Nachrichten*, 322:401–404, December 2001. doi: 10.1002/1521-3994(200112)322:5/6⟨401::AID-ASNA401⟩3.0.CO;2-M.

H. Edelmann, U. Heber, H. J. Hagen, M. Lemke, S. Dreizler, R. Napiwotzki, and D. Engels. Spectral analysis of sdB stars from the Hamburg Quasar Survey. , 400:939–950, March 2003. doi: 10.1051/0004-6361:20030135.

H. Edelmann, U. Heber, and R. Napiwotzki. Metal Abundances of SdB Stars. *Baltic Astronomy*, 15:103–106, January 2006.

R. F. Green, M. Schmidt, and J. Liebert. The Palomar-Green Catalog of Ultraviolet-Excess Stellar Objects. , 61:305, June 1986. doi: 10.1086/191115.

Philip D. Hall, Christopher A. Tout, Robert G. Izzard, and Denise Keller. Planetary nebulae after common-envelope phases initiated by low-mass red giants. , 435(3):2048–2059, November 2013. doi: 10.1093/mnras/stt1422.

Wolf-Rainer Hamann, Achim Feldmeier, and Lidia M Oskinova. Clumping in hot-star winds : proceedings of an international workshop held in potsdam, germany, 18. - 22. june 2007. 2008.

Z. Han, Ph. Podsiadlowski, P. F. L. Maxted, and T. R. Marsh. The origin of subdwarf B stars - II. , 341(2):669–691, May 2003. doi: 10.1046/j.1365-8711.2003.06451.x.

S. Hatchett and R. McCray. X-ray sources in stellar winds. , 211:552–561, January 1977. doi: 10.1086/154962.

U. Heber. Hot Subluminous Stars. , 128(966):082001, August 2016. doi: 10.1088/1538-3873/128/966/082001.

U. Heber and H. Edelmann. Atmospheric Parameters and Abundances of sdB Stars. , 291(3): 341–349, June 2004. doi: 10.1023/B:ASTR.0000044342.79287.fc.

U. Heber, I. N. Reid, and K. Werner. Spectral analysis of multi mode pulsating sdB stars. II. Feige 48, KPD 2109+4401 and PG 1219+534. , 363:198–207, November 2000. doi: 10.48550/arXiv.astro-ph/0009159.

U. Heber, H. Edelmann, T. Lisker, and R. Napiwotzki. Discovery of a helium-core white dwarf progenitor. , 411:L477–L480, December 2003. doi: 10.1051/0004-6361:20031553.

Ulrich Heber. Hot Subdwarf Stars. , 47(1):211–251, September 2009. doi: 10.1146/annurev-astro-082708-101836.

D. J. Hillier. The effects of electron scattering and wind clumping for early emission line stars. , 247:455, July 1991.

Heiko Hirsch and Uli Heber. Carbon abundances of sdO stars from SPY. In *Journal of Physics Conference Series*, volume 172 of *Journal of Physics Conference Series*, page 012015. IOP, June 2009. doi: 10.1088/1742-6596/172/1/012015.

Susanne Höfner and Hans Olofsson. Mass loss of stars on the asymptotic giant branch. Mechanisms, models and measurements. , 26(1):1, January 2018. doi: 10.1007/s00159-017-0106-5.

G. L. Israel, L. Stella, L. Angelini, N. E. White, T. R. Kallman, P. Giommi, and A. Treves. The Discovery of 13 Second X-Ray Pulsations from the Hydrogen-depleted Subdwarf O6 Star Binary HD 49798. , 474(1):L53–L56, January 1997. doi: 10.1086/310418.

N. Ivanova, S. Justham, X. Chen, O. De Marco, C. L. Fryer, E. Gaburov, H. Ge, E. Glebbeek, Z. Han, X. D. Li, G. Lu, T. Marsh, P. Podsiadlowski, A. Potter, N. Soker, R. Taam, T. M. Tauris, E. P. J. van den Heuvel, and R. F. Webbink. Common envelope evolution: where we stand and how we can move forward. , 21:59, February 2013. doi: 10.1007/s00159-013-0059-2.

Stephen Justham, Philipp Podsiadlowski, and Zhanwen Han. On the formation of single and binary helium-rich subdwarf O stars. , 410(2):984–993, January 2011. doi: 10.1111/j.1365-2966.2010.17497.x.

A. Kawka, S. Vennes, S. O'Toole, P. Németh, D. Burton, E. Kotze, and D. A. H. Buckley. New binaries among UV-selected, hot subdwarf stars and population properties. , 450(4):3514–3548, July 2015. doi: 10.1093/mnras/stv821.

R. I. Klein and J. I. Castor. H and He II spectra of Of stars. , 220:902–923, March 1978. doi: 10.1086/155980.

S. Klepp and T. Rauch. On the sdOB primary of the post common-envelope binary ¡ASTROBJ¿AA Doradus¡/ASTROBJ¿ (¡ASTROBJ¿LB 3459¡/ASTROBJ¿). , 531:L7, July 2011. doi: 10.1051/0004-6361/201116887.

J. Krtička, J. Janík, I. Krtičková, S. Mereghetti, F. Pintore, P. Németh, J. Kubát, and M. Vučković. Hot subdwarf wind models with accurate abundances. I. Hydrogen dominated stars HD 49798 and BD+18° 2647. , 631:A75, November 2019. doi: 10.1051/0004-6361/201936208.

J. Krtička. Horké hvězdy II. *á*, page 57, 2015.

R. P. Kudritzki and K. P. Simon. Non-LTE analysis of subluminous O-star. The hydrogen-deficient subdwarf O-binary HD 49798. , 70:653–663, November 1978.

T. Kupfer, S. Geier, U. Heber, R. H. Østensen, B. N. Barlow, P. F. L. Maxted, C. Heuser, V. Schaffenroth, and B. T. Gänsicke. Hot subdwarf binaries from the MUCHFUSS project. Analysis of 12 new systems and a study of the short-period binary population. , 576:A44, April 2015. doi: 10.1051/0004-6361/201425213.

H. J. G. L. M. Lamers. Intorduction to Stellar Winds. *University Press*, 1999. doi: //doi.org/10.1017/CBO9781139175012.

Henny J. G. L. M. Lamers and Claus Leitherer. What are the Mass-Loss Rates of O Stars? , 412:771, August 1993. doi: 10.1086/172960.

Thierry Lanz, Thomas M. Brown, Allen V. Sweigart, Ivan Hubeny, and Wayne B. Landsman. Flash Mixing on the White Dwarf Cooling Curve: Far Ultraviolet Spectroscopic Explorer Observations of Three He-rich sdB Stars. , 602(1):342–355, February 2004. doi: 10.1086/380904.

T. Lisker, U. Heber, R. Napiwotzki, N. Christlieb, Z. Han, D. Homeier, and D. Reimers. Hot subdwarfs from the ESO Supernova Ia Progenitor Survey. I. Atmospheric parameters and cool companions of sdB stars. , 430:223–243, January 2005. doi: 10.1051/0004-6361:20040232.

W. M. Liu, W. C. Chen, B. Wang, and Z. W. Han. Helium-star evolutionary channel to super-Chandrasekhar mass type Ia supernovae. , 523:A3, November 2010. doi: 10.1051/0004-6361/201014180.

P. Lorén-Aguilar, J. Isern, and E. García-Berro. High-resolution smoothed particle hydrodynamics simulations of the merger of binary white dwarfs. , 500(3):1193–1205, June 2009. doi: 10.1051/0004-6361/200811060.

L. B. Lucy and R. L. White. X-ray emission from the winds of hot stars. , 241:300–305, October 1980. doi: 10.1086/158342.

P. F. L. Maxted, U. Heber, T. R. Marsh, and R. C. North. The binary fraction of extreme horizontal branch stars. , 326(4):1391–1402, October 2001. doi: 10.1111/j.1365-2966.2001.04714.x.

P. F. L. Maxted, T. R. Marsh, U. Heber, L. Morales-Rueda, R. C. North, and W. A. Lawson. Photometry of four binary subdwarf B stars and the nature of their unseen companion stars. , 333(1):231–240, June 2002. doi: 10.1046/j.1365-8711.2002.05406.x.

Pierre F. L. Maxted, Luisa Morales-Rueda, and Tom R. Marsh. Companions to sdB binaries-degenerate or non-degenerate? , 291(3):307–314, June 2004. doi: 10.1023/B:ASTR.0000044337.19671.de.

S. Mereghetti, A. Tiengo, P. Esposito, N. La Palombara, G. L. Israel, and L. Stella. An Ultra-massive, Fast-Spinning White Dwarf in a Peculiar Binary System. *Science*, 325(5945):1222, September 2009. doi: 10.1126/science.1176252.

S. Mereghetti, N. La Palombara, A. Tiengo, F. Pizzolato, P. Esposito, P. A. Woudt, G. L. Israel, and L. Stella. X-ray and optical observations of the unique binary system hd 49798/rx j0648.0–4418. *The Astrophysical Journal*, 737(2):51, jul 2011. doi: 10.1088/0004-637X/737/2/51. URL https://dx.doi.org/10.1088/0004-637X/737/2/51.

S. Mereghetti, N. La Palombara, A. Tiengo, N. Sartore, P. Esposito, G. L. Israel, and L. Stella. X-ray emission from the luminous O-type subdwarf HD 49798 and its compact companion. , 553:A46, May 2013. doi: 10.1051/0004-6361/201321271.

S. Mereghetti, F. Pintore, T. Rauch, N. La Palombara, P. Esposito, S. Geier, I. Pelisoli, M. Rigoselli, V. Schaffenroth, and A. Tiengo. New X-ray observations of the hot subdwarf binary HD 49798/RX J0648.0-4418. , 504(1):920–925, June 2021. doi: 10.1093/mnras/stab1004.

Sandro Mereghetti and Nicola La Palombara. X-rays from hot subdwarfs. *Advances in Space Research*, 58(5):809–820, September 2016. doi: 10.1016/j.asr.2015.11.022.

Sandro Mereghetti, Fabio Pintore, Paolo Esposito, Nicola La Palombara, Andrea Tiengo, Gian Luca Israel, and Luigi Stella. Discovery of spin-up in the X-ray pulsar companion of the hot subdwarf HD 49798. , 458(4):3523–3527, June 2016. doi: 10.1093/mnras/stw536.

M. M. Miller Bertolami, L. G. Althaus, K. Unglaub, and A. Weiss. Modeling He-rich subdwarfs through the hot-flasher scenario. , 491(1):253–265, November 2008. doi: 10.1051/0004-6361:200810373.

M. R. Mokiem, A. de Koter, J. S. Vink, J. Puls, C. J. Evans, S. J. Smartt, P. A. Crowther, A. Herrero, N. Langer, D. J. Lennon, F. Najarro, and M. R. Villamariz. The empirical metallicity dependence of the mass-loss rate of O- and early B-type stars. , 473(2):603–614, October 2007. doi: 10.1051/0004-6361:20077545.

L. Morales-Rueda, P. F. L. Maxted, T. R. Marsh, R. C. North, and U. Heber. Orbital periods of 22 subdwarf B stars. , 338(3):752–764, January 2003. doi: 10.1046/j.1365-8711.2003.06088.x.

C. Moran, P. Maxted, T. R. Marsh, R. A. Saffer, and M. Livio. The orbital parameters of three new subdwarf B binaries. , 304(3):535–539, April 1999. doi: 10.1046/j.1365-8711.1999.02314.x.

R. Napiwotzki, N. Christlieb, H. Drechsel, H. J. Hagen, U. Heber, D. Homeier, C. Karl, D. Koester, B. Leibundgut, T. R. Marsh, S. Moehler, G. Nelemans, E. M. Pauli, D. Reimers, A. Renzini, and L. Yungelson. Search for progenitors of supernovae type Ia with SPY. *Astronomische Nachrichten*, 322:411–418, December 2001. doi: 10.1002/1521-3994(200112)322:5/6⟨411::AID-ASNA411⟩3.0.CO;2-I.

R. Napiwotzki, C. A. Karl, T. Lisker, U. Heber, N. Christlieb, D. Reimers, G. Nelemans, and D. Homeier. Close binary EHB stars from SPY. , 291(3):321–328, June 2004. doi: 10.1023/B:ASTR.0000044362.07416.6c.

Michael Nauenberg. Analytic Approximations to the Mass-Radius Relation and Energy of Zero-Temperature Stars. , 175:417, July 1972. doi: 10.1086/151568.

Stanley P. Owocki. Instabilities in the Envelopes and Winds of Very Massive Stars. In J. S. Vink, editor, *Very Massive Stars in the Local Universe*, volume 412 of *Astrophysics and Space Science Library*, page 113, January 2015. doi: 10.1007/978-3-319-09596-7_5.

Stanley P. Owocki, John I. Castor, and George B. Rybicki. Time-dependent Models of Radiatively Driven Stellar Winds. I. Nonlinear Evolution of Instabilities for a Pure Absorption Model. , 335:914, December 1988. doi: 10.1086/166977.

B. Paczynski. Common Envelope Binaries. In Peter Eggleton, Simon Mitton, and John Whelan, editors, *Structure and Evolution of Close Binary Systems*, volume 73 of *IAU Symposium*, page 75, January 1976.

Michael Politano, Ronald E. Taam, Marc van der Sluys, and Bart Willems. Common-Envelope Mergers: A Possible Channel for Forming Single sdB Stars. , 687(2):L99, November 2008. doi: 10.1086/593328.

S. B. Popov, S. Mereghetti, S. I. Blinnikov, A. G. Kuranov, and L. R. Yungelson. A young contracting white dwarf in the peculiar binary HD 49798/RX J0648.0-4418? , 474(2):2750–2756, February 2018. doi: 10.1093/mnras/stx2910.

D. Pourbaix, A. A. Tokovinin, A. H. Batten, F. C. Fekel, W. I. Hartkopf, H. Levato, N. I. Morrell, G. Torres, and S. Udry. $S_B{}^9$: $The ninth catalogue of spectroscopic binary orbits.$ ,$424 : 727 - -732, September 2004. doi :$ .

Raman K. Prinja, M. J. Barlow, and Ian D. Howarth. Terminal Velocities for a Large Sample of O Stars, B Supergiants, and Wolf-Rayet Stars. , 361:607, October 1990. 10.1086/169224.

J. Puls, R. P. Kudritzki, A. Herrero, A. W. A. Pauldrach, S. M. Haser, D. J. Lennon, R. Gabler, S. A. Voels, J. M. Vilchez, S. Wachter, and A. Feldmeier. O-star mass-loss and wind momentum rates in the Galaxy and the Magellanic Clouds Observations and theoretical predictions. , 305:171, January 1996.

Joachim Puls, J. S. Vink, and Francisco Najarro. Mass loss from hot massive stars. , 16(3-4):209–325, December 2008. 10.1007/s00159-008-0015-8.

T. Rauch, A. Rudkowski, D. Kampka, K. Werner, J. W. Kruk, and S. Moehler. The virtual observatory service TheoSSA: Establishing a database of synthetic stellar flux standards . II. NLTE spectral analysis of the OB-type subdwarf ¡ASTROBJ¿Feige 110¡/ASTROBJ¿. , 566:A3, June 2014. 10.1051/0004-6361/201423711.

Thomas Rauch, Klaus Werner, and Jeffrey W. Kruk. EC 11481–2303—a peculiar subdwarf OB star revisited. , 329(1-2):133–139, October 2010. 10.1007/s10509-010-0304-3.

Michela Rigoselli, Davide De Grandis, Sandro Mereghetti, and Christian Malacaria. Timing the X-ray pulsating companion of the hot subdwarf HD 49798 with NICER. , 523(2):3043–3048, August 2023. 10.1093/mnras/stad1611.

Rex A. Saffer, Mario Livio, and Lev R. Yungelson. Close Binary White Dwarf Systems: Numerous New Detections and Their Interpretation. , 502(1):394–407, July 1998. 10.1086/305907.

V. V. Shimanskii, I. F. Bikmaev, N. V. Borisov, V. V. Vlasyuk, A. I. Galeev, N. A. Sakhibullin, and O. I. Spiridonova. Spectral types of four binaries based on photometric observations. *Astronomy Reports*, 52(9):729–735, September 2008. 10.1134/S1063772908090047.

Noam Soker. Can Planets Influence the Horizontal Branch Morphology? , 116(3):1308–1313, September 1998. 10.1086/300503.

Allen V. Sweigart. Evolutionary Sequences for Horizontal-Branch Stars. , 65:95, September 1987. 10.1086/191219.

Allen V. Sweigart. Effects of Helium Mixing on the Evolution of Globular Cluster Stars. , 474(1): L23–L26, January 1997a. 10.1086/310414.

Allen V. Sweigart. Helium Mixing in Globular Cluster Stars. In A. G. D. Philip, J. Liebert, R. Saffer, and D. S. Hayes, editors, *The Third Conference on Faint Blue Stars*, page 3, January 1997b. 10.48550/arXiv.astro-ph/9708164.

Marco Tailo, Francesca D'Antona, Enrico Vesperini, Marcella di Criscienzo, Paolo Ventura, Antonino P. Milone, Andrea Bellini, Aaron Dotter, Thibaut Decressin, Annibale D'Ercole, Vittoria Caloi, and Roberto Capuzzo-Dolcetta. Rapidly rotating second-generation progenitors for the 'blue hook' stars of $\omega$ Centauri. , 523(7560):318–321, July 2015. 10.1038/nature14516.

A. D. Thackeray. The spectroscopic orbit of the O-type subdwarf HD 49798. , 150:215, January 1970. 10.1093/mnras/150.2.215.

J. S. Vink. *Radiation-driven Wind Models of Massive Stars*. PhD thesis, University of Utrecht, Netherlands, November 2000.

J. S. Vink. Theory and diagnostics of hot star mass loss. *Annual Review of Astronomy and Astrophysics*, 60(Volume 60, 2022):203–246, 2022. ISSN 1545-4282. https://doi.org/10.1146/annurev-astro-052920-094949. URL https://www.annualreviews.org/content/journals/10.1146/annurev-astro-052920-094949.

J. S. Vink. Stellar Winds. *arXiv e-prints*, art. arXiv:2406.1 6517, June 2024. 10.48550/arXiv.2406.16517.

Jorick S. Vink. Theory and Diagnostics of Hot Star Mass Loss. , 60:203–246, August 2022. 10.1146 /annurev-astro-052920 -094949.

R. F. Webbink. Double white dwarfs as progenitors of R Coronae Borealis stars and type I supernovae. , 277:355–360, February 1984. 10.1086/161701.

Xianfei Zhang and C. Simon Jeffery. Evolutionary models for double helium white dwarf mergers and the formation of helium-rich hot subdwarfs. , 419(1):452–464, January 2012. 10.1111/j.1365-2966.2011.19711.x.